Modélisation empirique de l'évolution des galaxies infrarouges

Sommaire

6.1 Introduction

La plupart des observables infrarouges (comptages, N(z)...) n'apportent pas une information directe sur l'évolution des galaxies. Par exemple, Sect. 2.1.2, nous avons vu comment celle-ci agit de manière non triviale sur les comptages de sources. Pour interpréter ces différentes observations, il est donc nécessaire de recourir à un modèle, qui peut se construire selon plusieurs approches. La première, dite semi-analytique, a pour but de retrouver l'évolution observée grâce à une modélisation purement physique. La seconde, dite *backward evolution*[1], est plus empirique et tente de reproduire finement les observations grâce à une évolution plus ou moins simple des propriétés statistiques des objets. J'ai développé au cours de ma thèse un modèle de type *backward evolution*.

6.1.1 Modèles semi-analytiques

Les modèles semi-analytiques se basent sur les grandes simulations d'effondrement de la matière noire (par exemple la simulation Millenium, Springel *et al.* (2005)). Elles partent des très faibles fluctuations de densité (de l'ordre de 10^{-5}) observées dans le fond cosmologique, et simulent la manière dont ces fluctuations croissent sous l'effet de la gravité pour former les halos de matière noire. Ceci fournit l'historique de la croissance par accrétion et fusions éventuelles de tous les halos présents dans le volume d'Univers simulé. Des recettes semi-analytiques permettent alors de décrire l'effondrement et le refroidissement du gaz dans les halos, qui permet la formation d'étoiles. Ce mécanisme est piloté par le temps d'effondrement dynamique et le temps de refroidissement du milieu interstellaire.

Pour pouvoir comparer ces simulations aux données, il faut également simuler le spectre de chaque galaxie. La distribution en masse des étoiles crées à chaque pas de la simulation est donnée par la fonction de masse initiale (IMF[2]). On peut citer, entre autres, les IMFs de Salpeter (1955), Kroupa (2001) et Chabrier (2003). A chaque pas de la simulation, on calcule alors la distribution en masse et en âge des étoiles. La distribution spectrale d'énergie (SED) totale émise par les populations stellaires peut ainsi être déterminée en utilisant des *templates* comme ceux de Bruzual et Charlot (2003). On prend ensuite en compte l'extinction du spectre par la poussière. L'énergie ainsi absorbée est alors émise dans l'infrarouge.

Il existe de nombreux modèles semi-analytiques construit sur des hypothèses différentes, comme par exemple, Hatton *et al.* (2003), Somerville *et al.* (2008), ou Lacey *et al.* (2010). Aujourd'hui, ces modèles sont encore incapables de reproduire fidèlement les observations infrarouges sans modifier l'IMF. Les taux de formation d'étoiles sont trop

---

[1]En français, évolution à rebours.

[2]De l'anglais, *Initial Mass Function*

faibles à haut *redshift* pour engendrer suffisamment d'ULIRGs à z=2. Les modèles utilisent en général une IMF modifiée avec plus d'étoiles massives que dans celle de Salpeter (1955) pour régler ce problème. En effet, si les étoiles sont plus massives, elles sont plus bleues. Leur lumière est donc plus absorbée, ce qui augmente mécaniquement la luminosité infrarouge pour un même taux de formation d'étoiles. Cette modification de l'IMF sans grande motivation physique n'est néanmoins pas très satisfaisante. Une meilleure prise en compte des courants de gaz froid le long des filaments de matière noire ou de la *clumpiness*[3] pourrait permettre de régler ce problème.

6.1.2 Modèles *backward evolution*

L'approche dite *backward evolution* consiste à faire évoluer au cours du temps les propriétés statistiques des galaxies infrarouges comme la fonction de luminosité. Ces propriétés sont en général bien contraintes dans l'Univers local. Elles le sont beaucoup moins dans l'Univers lointain. Ces modèles partent donc en général des propriétés observées localement et les font évoluer avec le *redshift*, d'où le terme *backward evolution*.

Il existe de très nombreux modèles de type *backward evolution*. Chacun se construit sur des hypothèses assez différentes. Nous présentons ici une sélection de modèles récents.

Modèle de Lagache *et al.* (2003, 2004)

Le modèle de Lagache *et al.* (2003, 2004) utilise deux populations évoluant indépendamment pour reproduire les comptages de l'infrarouge moyen au domaine sub-millimétrique. Ces deux populations sont les galaxies passives froides et les galaxies à flambée de formation d'étoiles (*starburst*). Les distributions spectrales d'énergie des galaxies à flambée de formation d'étoiles évoluent avec la luminosité infrarouge : plus elles sont lumineuses et plus elles sont chaudes. Leur densité et leur luminosité caractéristiques évoluent très rapidement avec le *redshift*. Les SEDs des galaxies froides n'évoluent pas, quant à elles, en fonction de la luminosité. La LF de cette population évolue peu avec le *redshift*. Ces évolutions sont déterminées manuellement par essais successifs jusqu'à reproduire les observations.

---

[3]Ce mot difficile à traduire en français signifie que le gaz n'est pas réparti de manière uniforme, mais en paquets.

Modèle de Negrello *et al.* (2007)

Le modèle de Negrello *et al.* (2007) est construit de façon très différente. Il contient une population de galaxies sphéroïdales à haut *redshift* formant des étoiles à un rythme très soutenu. Leur évolution est décrite par le modèle physique de Granato *et al.* (2004). Une population de galaxies spirales formant leurs étoiles à un rythme plus modéré est ajouté de façon purement empirique afin d'ajuster les observations. Les radio-galaxies du modèle de de Zotti *et al.* (2005) sont également ajoutées à ce modèle. Enfin, il contient une population de galaxies sphéroïdales amplifiée par effet de lentille gravitationnelle (Perrotta *et al.* (2002)). Ces sources lentillées ont un effet important sur les comptages de sources dans le domaine sub-millimétrique pour des flux de l'ordre de 100 mJy. La prise en compte de ce phénomène est une particularité importante de ce modèle.

Modèle de Le Borgne *et al.* (2009)

Le modèle de Le Borgne *et al.* (2009) est un modèle empirique basé sur une seule population, qui correspond à la bibliothèque de SED de Chary et Elbaz (2001). Cette bibliothèque évolue uniquement avec la luminosité infrarouge. L'originalité de ce modèle réside dans la façon dont est déterminée l'évolution des galaxies infrarouges. Il ne suppose pas une forme paramétrique particulière pour la fonction de luminosité, mais force la fonction de luminosité à évoluer lentement en fonction de la luminosité et du *redshift*. Les évolutions de la LF compatibles avec les comptages infrarouges sont déterminées de façon automatique.

Modèle de Valiante *et al.* (2009)

Le modèle de Valiante *et al.* (2009) utilise une stratégie assez différente. Il prend en compte les variations de température des grains et de contribution AGN entre galaxies. Il tire aléatoirement des *templates* de galaxies pour construire un catalogue simulé qui est ensuite utilisé pour prédire les différentes observables infrarouges. Les paramètres de ce modèle sont choisis manuellement afin reproduire de manière satisfaisante les observations. Les auteurs prétendent que la prise en compte des AGN est absolument nécessaire pour reproduire les comptages infrarouges.

Modèle de Franceschini *et al.* (2010)

Le modèle de Franceschini *et al.* (2010) utilise plusieurs populations ayant chacune sa propre évolution : spirales, AGNs, LIRGs et ULIRGs. L'évolution de chaque population est déterminée manuellement afin de reproduire au mieux les observations. Grâce à son

très grand nombre de paramètres libres, ce modèle est fréquemment revisité afin de toujours reproduire les observations.

6.1.3   Vers une nouvelle génération de modèles *backward evolution*

Des observations récentes mettent à mal les modèles cités précédemment. Deux observations à elles-seules éliminent l'ensemble des modèles pré-*Herschel*.

La première est la mesure des comptages observés avec SPIRE (Oliver *et al.* (2010)). A l'exception du modèle de Valiante *et al.* (2009) et Negrello *et al.* (2007), tous les modèles surestimenent les comptages de sources à haut flux (c.f. Fig. 6.1 gauche). Le modèle de Negrello *et al.* (2007) surestime toutefois les comptages autour de 50 mJy. Seul le modèle de Valiante *et al.* (2009) est en bon accord avec cette observable.

Une autre mesure très discriminante a été réalisée. Il s'agit de la contribution des sources détectées à 24 μm au fond infrarouge en fonction du *redshift* (c.f. Fig. 6.1 droite et Sect. 5.2.1). Le modèle de Valiante *et al.* (2009) est en complet desaccord avec cette mesure.

Aucun des modèles pré-*Herschel* n'a été donc en mesure de prédire ces nouvelles observables. Bien entendu, certains de ces modèles pourrait être légèrement modifiés pour mieux reproduire les nouvelles contraintes. Néanmoins, la modification permenante d'évolutions introduites "à la main" pour ajuster chaque nouvelle observation est-elle réellement satisfaisante ? De plus, nombre de ces modèles ont un très grand nombre de paramètres libres cachés (par exemple, plus de 40 pour le modèle Lagache *et al.* (2004)). La construction d'un modèle simple reproduisant la plupart des observations serait bien plus satisfaisante qu'une compléxification d'un modèle ancien. C'est cette considération qui m'a poussé à construire un nouveau modèle paramétrique ajusté directement sur les observations.

Nous présentons ici un bref résumé du travail de modélisation que j'ai effectué. Le détail de ce travail est fourni dans l'article en fin de chapitre (Béthermin *et al.* (2011)).

6.2   Description du nouveau modèle

Ce nouveau modèle est purement paramétrique (13 paramètres libres). Il s'inspire du modèle de Lagache *et al.* (2004), mais limite grandement le nombre de paramètres à ajuster. Il n'utilise pas d'AGNs.
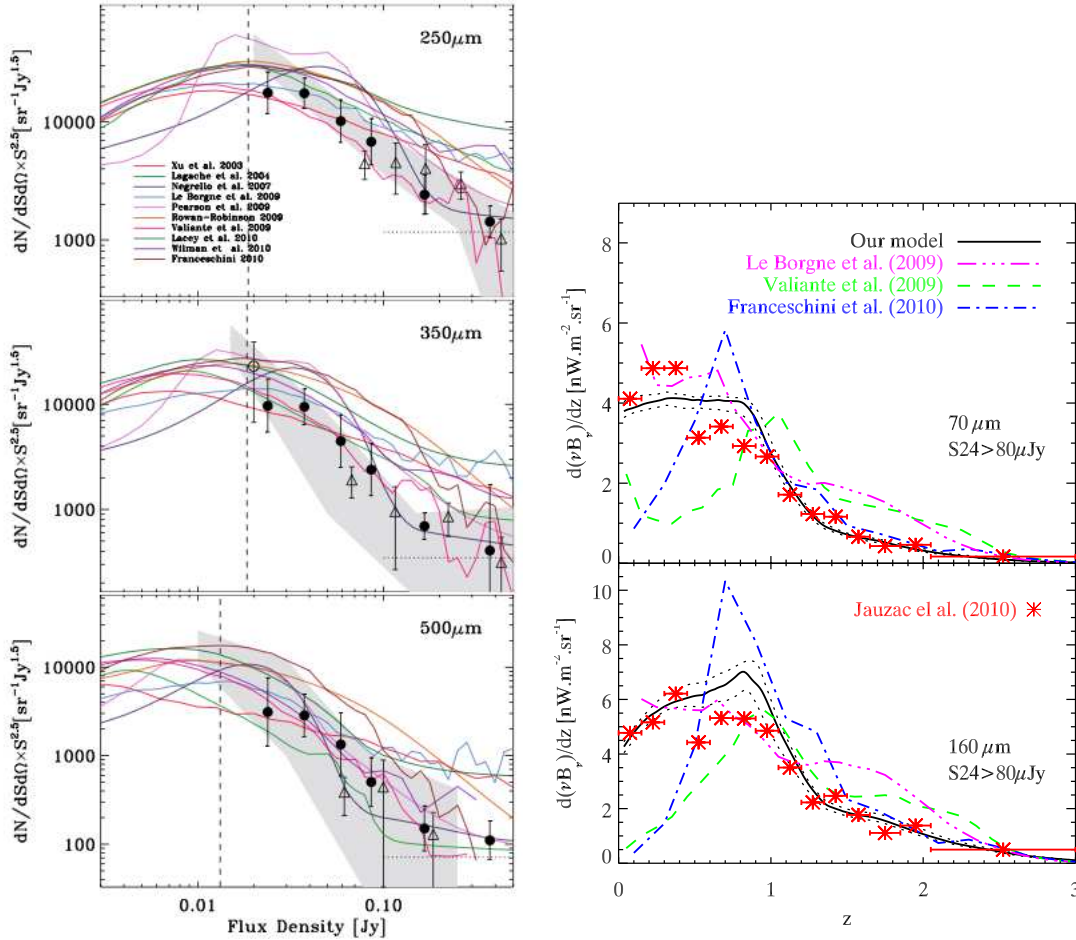
FIGURE 6.1 – (À gauche) Comptages extragalactiques à 250, 350 et 500 μm mesurés par Oliver *et al.* (2010) (cercles pleins), Béthermin *et al.* (2010b) (triangles ouverts), Khan *et al.* (2007) (cercles ouverts) et Patanchon *et al.* (2009) (zone grisée). Figure de Oliver *et al.* (2010). Les lignes colorées représentent différents modèles de galaxies. (À droite) Contribution des sources détectées à 24 μm au CIB en fonction du *redshift*. Les astérisques rouges correspondent aux mesures de Jauzac *et al.* (2011) par stacking. Les prédictions de différents modèles sont représentées : Le Borgne *et al.* (2009) (tirets-3 points violet), Valiante *et al.* (2009) (tirets verts), Franceschini *et al.* (2010) (tirets-points bleus) et Béthermin *et al.* (2011) (ligne pleine noire).

Les paramètres cosmologiques utilisés sont ceux du modèle ΛCDM ajusté sur les données WMAP 7 ans (Larson *et al.*, 2010). Nous avons donc $H_0 = 71$ km.s^{-1}.Mpc^{-1}, Ω_Λ = 0.734 and Ω_m = 0.266.

6.2.1   Fonction de luminosité et son évolution

Nous utilisons dans ce modèle une fonction de luminosité (LF) infrarouge de la forme classique (Saunders *et al.*, 1990) :

$$\Phi(L_{IR}) = \Phi^{\star} \times (\frac{L_{IR}}{L^{\star}})^{1-\alpha} \times exp[-\frac{1}{2\sigma^2}log_{10}^2(1 + \frac{L_{IR}}{L^{\star}}))] \tag{6.1}$$

où $\Phi(L_{IR})$ est le nombre de source par dex et par unité de volume comobile à une luminosité bolométrique infrarouge donnée L_{IR} donnée. $\Phi_\star$ et $L_\star$ caractérisent la densité et la luminosité caractéristiques à la coupure de la LF. α et σ régissent le comportement à basse et haute luminosité.

Pour reproduire les observations infrarouges, nous autorisons les paramètres de la fonction de luminosité à évoluer avec le *redshift*. Pour limiter le nombre de paramètres libres et également éviter de créer de fortes dégénérescences, nous fixons α et σ. L'évolution des autres paramètres est de la forme $L^{\star} \propto (1 + z)^{r_L}$ et $\Phi^{\star} \propto (1 + z)^{r_\Phi}$, un unique jeu de r_L et r_Φ ne pouvant permettre de reproduire les observations. Nous utilisons trois valeurs distinctes de r_L et r_Φ à bas (0 à z_{break}), moyen (z_{break} et 2) et haut *redshift* (plus de 2). z_{break} est un paramètre libre qui s'ajuste naturellement, en revanche nous fixons la second changement d'exposant à z=2, celui-ci n'aparaissant pas naturellement.

6.2.2   Distributions spectrales d'énergie

Pour construire ce modèle, nous utilisons les bibliothèques de distribution spectrale d'énergie de Lagache *et al.* (2004) (c.f. Sect. 6.1.2). Nous rappelons que cette bibliothèque contient deux familles : les galaxies foides passives (type spirale) et les galaxies à flambée de formation d'étoiles.

Les galaxies froides sont dominantes à faible luminosité infrarouge et les galaxies à flambées de formation d'étoiles le sont à forte luminosité. Nous avons choisi arbitrairement de décrire la fraction de galaxies à flambée de formation d'étoiles en fonction de la luminosité totale infrarouge L_{IR} de la manière suivante :

$$\frac{\Phi_{starburst}}{\Phi} = \frac{1 + th[log_{10}(L_{IR}/L_{pop})/\sigma_{pop}]}{2} \tag{6.2}$$

où *th* est la fonction tangente hyperbolique. L_{pop} est la luminosité pour laquelle les contributions des deux populations sont égales. σ_{pop} caractérise la largeur de la transition entre les deux populations.

6.2.3 Effet des lentilles gravitationnelles sur les observables

En relativité générale, les fortes masses ont la faculté de courber les rayons lumineux. Les fortes concentrations de matière peuvent ainsi agir à la façon d'un lentille optique. On parle alors de lentilles gravitationnelles. Les halos des galaxies elliptiques massives proches peuvent amplifier le flux de galaxies lointaines (Perrotta *et al.*, 2001, 2002). Ce phénomène peut modifier significativement les comptages lorsque leur pente est forte. Pour prendre en compte ce phénomène dans le modèle nous utilisons un modèle simple supposant que les halos de matière noire sont des sphères isothermes, qui détermine comment les lentilles modifient les comptages.

6.3 Ajustement des observations

6.3.1 Sélection des données à ajuster

Une quantité colossale de mesures a été réalisée dans l'infrarouge : comptages, fonctions de luminosité, distribution en *redshift*, couleurs des sources... Néanmoins, ces différentes observations sont plus ou moins affectées par des biais d'analyse et/ou de sélection. Les comptages sont par nature peu biaisés, si les effets d'extraction sont bien corrigés. Néanmoins, de nombreux comptages publiés ne prennent pas en compte la variance cosmique. Ceci a guidé nos choix de comptages à ajuster. Nous avons également utilisé des fonctions de luminosité monochromatiques peu K-corrigées[4] dans le but de mieux contraindre le modèle. Une discussion détaillée sur le choix des points à ajuster est faite dans Béthermin *et al.* (2011).

La liste des observations sélectionnées est la suivante :

- Comptages *Spitzer*/MIPS de Béthermin *et al.* (2010a) à 24, 70 et 160 μm,

- Comptages *Herschel*/SPIRE de Oliver *et al.* (2010) à 250, 350 et 500 μm,

- Comptages AzTEC de Austermann *et al.* (2010) and Scott *et al.* (2010) at 1.1 mm.

- Fonction de luminosité locale IRAS à 60 μm de Saunders *et al.* (1990)

- Fonction de luminosité locale *Spitzer* à 24 μm de Rodighiero *et al.* (2009),

---

[4]Typiquement LF à $\lambda_{rest}/(1 + z)\mu$m déterminée à partir de donnée à λ_{rest}.

- Fonction de luminosité *Spitzer* à 15 μm à z=0.6 de Rodighiero *et al.* (2009),

- Fonction de luminosité *Spitzer* à 12 μm à z=1 de Rodighiero *et al.* (2009),

- Fonction de luminosité *Spitzer* à 8 μm at z=2 de Caputi *et al.* (2007),

- Fond infrarouge mesuré avec FIRAS par Lagache *et al.* (1999).

6.3.2 Ajustement

La calibration des instruments infrarouges n'étant pas parfaite, il faut la prendre en compte lors de l'ajustement des données. Cette incertitude, dépendant de l'instrument et de la bande, varie entre 4% et 15% (Stansberry *et al.* (2007), Gordon *et al.* (2007), Engelbracht *et al.* (2007), Swinyard *et al.* (2010)). Une modification de la calibration translate tous les comptages en x et en y : $S' = \gamma S$ et $(S'^{2.5}dN/dS') = \gamma^{1.5}(S^{2.5}dN/dS)$, où γ est un facteur qui vaut 1 si la calibration est parfaite.

Nous supposons que les incertitudes de mesure et de calibration sont toutes gaussiennes et non-corrélées. La vraissemblence L est donc donnée par :

$$-log(L(\theta)) = \sum_{k=1}^{Npoints} \frac{(m_k - m_{model,k}(\theta))^2}{2\sigma_m^2} + \sum_{b=1}^{Nband} \frac{(\gamma_b - 1)^2}{2\sigma_{calib,b}^2} \tag{6.3}$$

où θ est le vecteur contenant les paramètres du modèle, m_k une mesure, $m_{model,k}$ la prédiction du modèle pour la même mesure, σ_m l'incertitude sur cette mesure, γ_b le paramètre de calibration dans la bande b et $\sigma_{calib,b}$ l'incertitude de calibration dans cette bande.

Le modèle contient un nombre important de paramètres à ajuster et la densité de probabilité *a posteriori* n'a aucune raison d'être gaussienne. Pour cette raison, j'ai choisi d'utiliser la méthode *Monte Carlo Markov Chain* (MCMC). Notre meilleur ajustement a un χ^2 de 177 pour 113 degrés de liberté. Cet ajustement est donc relativement bon.

6.4 Résultats

6.4.1 Comparaison avec les observations

Le modèle ajuste de façon satisfaisante notre sélection de comptages à 24, 70, 160, 250, 350, 500 et 1100 μm (voir une sélection Fig. 6.2). Il sous-estime néanmoins légèrement les comptages à 24 μm (environ 10%) autour de 300 μJy. Bien qu'en accord à 1-σ avec les points de Oliver *et al.* (2010) que nous avons ajustés, les comptages prédits par le modèle sont systématiquement plus bas que les mesures à 350 et 500 μm. Le désaccord avec les
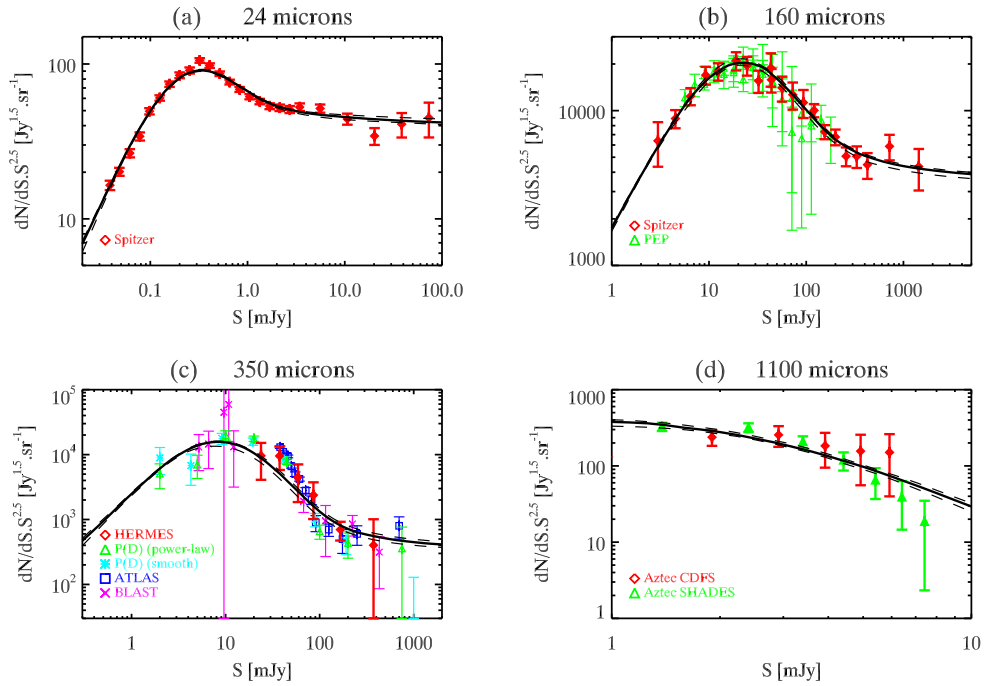
FIGURE 6.2 – Comptages infrarouge différentes longueurs d'onde comparées au modèle (ligne noire). (a) : Comptages à 24 μm de Béthermin *et al.* (2010a) (losanges rouges). (b) : Comptages à 160 μm de Béthermin *et al.* (2010a) (losanges rouges) et Berta *et al.* (2010) (triangles verts). (c) : Comptages à 350 μm de Béthermin *et al.* (2010b) (croix violettes), de Oliver *et al.* (2010) (losanges rouges), de Clements *et al.* (2010) (carrs bleus) et de Glenn *et al.* (2010) (triangles verts et astérisques bleues ciel). (d) : Comptages à 1.1 mm de Austermann *et al.* (2010) (losanges rouges) et de Scott *et al.* (2010) (triangles verts).

points de Clements *et al.* (2010) est plus grand. Toutefois, leurs points ne prennent pas en compte la variance cosmique. Les points P(D) ne doivent pas, quant à eux, être directement comparés au modèle comme expliqué dans le Chap. 4. L'ajustement du modèle directement sur l'histogramme des pixels des cartes SPIRE pourrait permettre à moyen terme de bien mieux contraindre le modèle dans les bandes SPIRE.

Le modèle peut également être comparé avec les comptages à d'autres longueurs d'onde : 15, 60, 100 et 850 μm. Les points expériementaux sont souvant en large désaccord entre eux. Néanmoins, le modèle passe dans le nuage de points à ces quatre longueurs d'onde. Nous avons également comparé nos comptages avec les comptages SPT de Vieira *et al.* (2009) à 1.4 mm. Notre modèle ne prend pas en compte les radio-galaxies (modélisées avec précision par le modèle de de Zotti *et al.* (2005)). Toutefois, la couleur 1.4 mm/2 mm des sources synchrotrons est très différente des galaxies infrarouges. Nous avons donc comparé les prédictions du modèle avec les comptages de sources "poussiéreuses" rouges de Vieira *et al.* (2009). L'accord est très bon. Nous avons également un très bon accord avec les comptages de sources sans contrepartie IRAS à 60 μm. Le modèle prédit qu'une grande partie de ces sources sont des galaxies amplifiées par effet de lentille gravitationnelle.

La distribution en *redshift* des sources sélectionnées en flux infrarouge est une contrainte importante pour le modèle. Néanmoins, ces contraintes peuvent être biaisées par le processus d'identification des contreparties optiques. Nous avons comparé les prédictions du modèle avec les observations pour différentes sélections : $S_{24} > 80\ \mu$Jy, $S_{24} > 300\ \mu$Jy, $S_{250} > 40$ mJy, $S_{350} > 30$ mJy, $S_{500} > 20$ mJy, $S_{850} > 3$ mJy, $S_{1100} > 3$ mJy. Pour les sélections à 24 μm, le modèle a tendance à surestimer le nombre de sources à bas *redshifts* ($z < 0.5$) et sous-estimer le nombre de sources à haut *redshifts* ($z > 2.5$) par rapport aux observations (Desai *et al.* (2008), Le Floc'h *et al.* (2009), Rodighiero *et al.* (2009)). Il y a un très bon accord avec les observations pour les sélections dans le domaine submillimétrique et millimétrique (Chapman *et al.* (2005); Chapin *et al.* (2009b, 2010)).

Les comptages prédits par le modèle permettent de calculer l'histogramme attendu des cartes BLAST. Ceci permet de tester la validité du modèle à bas flux. Il y a un très bon accord à 250 et 350 μm, en revanche le modèle prédit un pic légèrement trop étroit à 500 μm. Ce résultat est cohérant avec le fait que les comptages du modèle sont en dessous des observations 500 μm.

6.4.2 Histoire de la formation d'étoiles

Le modèle d'évolution permet de prédire la densité de luminosité bolométrique infrarouge ρ_{IR}, c'est-à-dire la puissance totale rayonnée en infrarouge par unité de volume comobile.
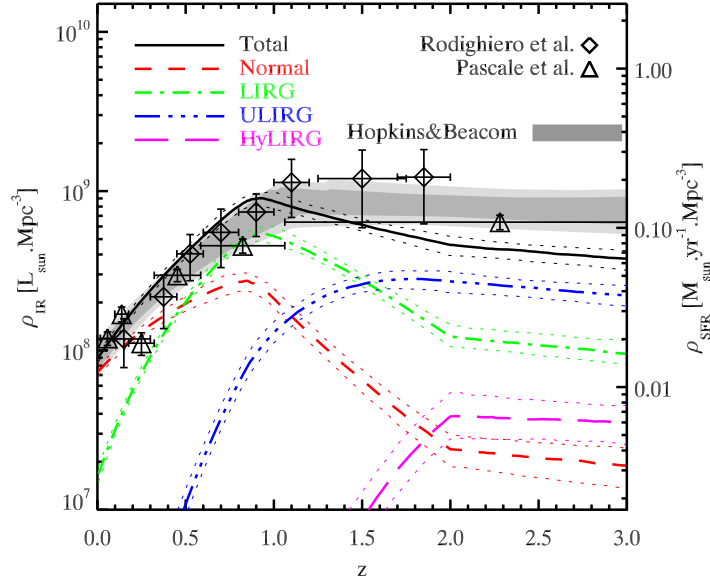
FIGURE 6.3 – Densité de luminosité infrarouge en fonction du *redshift* (en noir), et contribution des galaxies normales (rouge), des LIRGs (vert), ULIRG (bleu) et HyLIRG (violet). Comparaison avec les observations de Pascale *et al.* (2009), Rodighiero *et al.* (2009) et la compilation de Hopkins et Beacom (2006).

Cette grandeur peut être convertie en densité de formation d'étoiles grâce à la constante de Kennicutt qui vaut $1.7{\times}10^{-10}$ $M_\odot.yr^{-1}.L_\odot^{-1}$ (Kennicutt (1998)). La Fig. 6.3 réprésente l'évolution de ces deux quantités en fonction du *redshift*. On trouve que la densité de luminosité infrarouge (ainsi que la formation d'étoiles) augmente fortement jusqu'à z~1. On passe ainsi de 10^8 $L_\odot.Mpc^{-3}$ à 10^9 $L_\odot.Mpc^{-3}$ entre l'Univers local et z~1. La densité infrarouge décroît ensuite lentement avec le *redshift*. Cette évolution est en relatif accord avec les observations (Rodighiero *et al.* (2009), Pascale *et al.* (2009), Hopkins et Beacom (2006)).

Si on sépare les galaxies en différentes classes de luminosité, on constate que les galaxies normales dominent la densité infrarouge dans l'Univers local, alors qu'elle est dominée par les LIRGs à z=1 et les ULIRGs à z=2. Ceci montre que la formation d'étoiles a lieu dans des conditions physiques très différentes aujourd'hui et dans l'Univers jeune. Ceci pourrait s'expliquer par l'effondrement de gaz froid sur les halos les plus massifs à haut *redshift*.
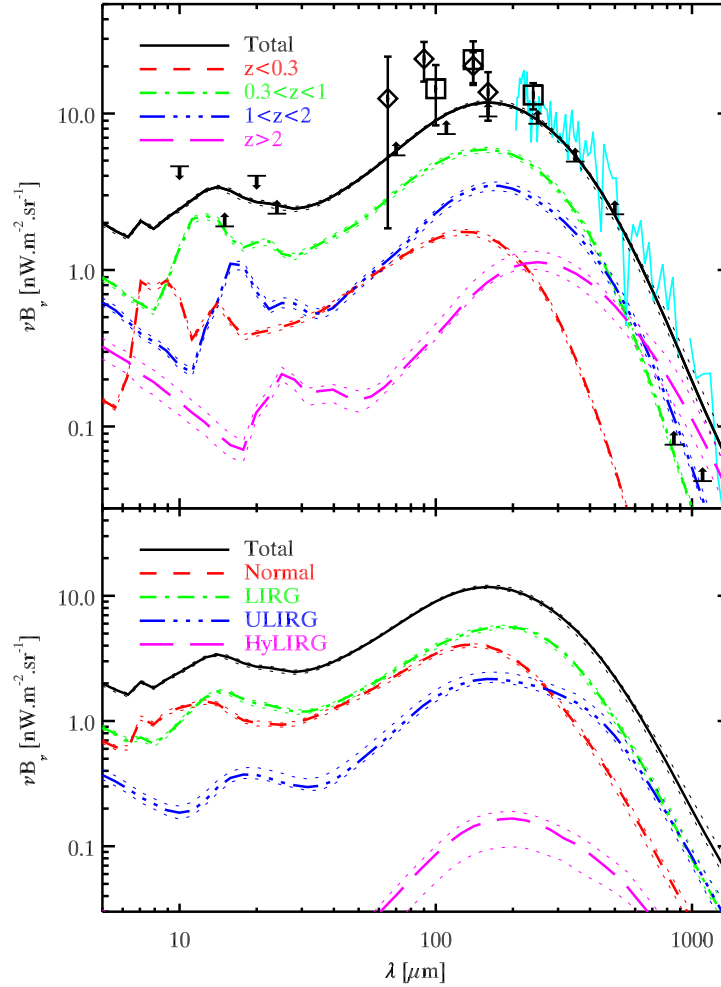
FIGURE 6.4 – Distribution spectrale d'énergie du fond infrarouge. Le fond total prédit par le modèle est en noir. (En haut) : Contribution des différentes tranches de *redshift* ($0 < z < 0.3$ en rouge, $0.3 < z < 1$ en vert, $1 < z < 2$ en bleu et $z > 2$ en violet). Les limites inférieures (comptages et/ou stacking) au fond sont représentées par des flèches vers le haut (Hopwood *et al.* (2010); Béthermin *et al.* (2010a); Berta *et al.* (2010); Marsden *et al.* (2009); Greve *et al.* (2009); Scott *et al.* (2010)). Les limites supérieures au fond (TeV) sont représentées par des flèches vers le bas (Stecker et de Jager (1997); Renault *et al.* (2001)). Les mesures absolues de DIRBE et *Akari* sont matérialisées par des carrés et des losanges, respectivement. Le spectre du fond infrarouge observé par FIRAS est en cyan (Lagache *et al.* (2000)). (En bas) : Contribution au fond des galaxies normales (rouge), des LIRGs (vert), des ULIRG (bleu) et des HyLIRG (violet).

6.4.3 Fond infrarouge

Le modèle peut également prédire la distribution spectrale d'énergie du fond infrarouge (voir Fig. 6.4). Le résultat est en bon accord avec les observations. On peut également séparer le fond infrarouge en tranches de *redshift*. On remarque qu'en dessous de 500 μm, la contribution dominante correspond à la tranche de *redshift* 0.3<z<1. En revanche, aux plus grandes longueurs d'onde, le fond est émis en majorité par des sources à z>2. En fait, plus on va vers les grandes longueurs d'onde, et plus on sonde les populations à haut *redshift*. Ceci est en accord avec les observations présentées Sect. 5.2.1

6.5 Conclusion

Nous avons montré dans ce chapitre qu'il est possible de reproduire avec succès les comptages infrarouges grâce à un modèle relativement simple. Ceci suggère que des modèles complexes utilisant un grand nombre de populations ne sont pas nécessaires pour reproduire les observations actuelles. Le nouveau modèle est le premier modèle d'évolution des galaxies infrarouges paramétriques, dont les paramètres sont déterminés par la méthode MCMC. Le même type de travail a été réalisé parallèlement[5] par Marsden *et al.* (2010). Les évolutions de la densité de luminosité infrarouge prédites par les deux modèles sont très différentes, alors que ces deux modèles reproduisent tout deux les comptages. Ceci montre qu'à l'avenir l'utilisation de nouvelles observables (comme les distribution en *redshift*) va être nécessaire pour discriminer les modèles.

Ce travail de modélisation pose également des questions importantes sur les processus de formation d'étoiles à grand *redshift*. En effet, nous avons trouvé que les ULIRGs dominent la formation d'étoiles à z=2. Dans l'Univers local, ce type de sources ne peut être dû qu'à une fusion majeure. Dans l'Univers lointain, les ULIRGs pourraient avoir un mécanisme très différent, basé sur une accrétion rapide de gaz froid. Ainsi, avec une approche globale, nous avons identifié une population d'objets surprenante. L'étude fine de leur physique devrait lever le voile sur la manière dont la majorité des étoiles se sont formées dans l'Univers jeune. Enfin, ce nouveau modèle permet de réaliser de nombreuses prédictions (limite de confusion, comptages...), qui devraient être très utiles pour préparer les relevés du futur. Elles sont également très utiles pour interpréter les récentes mesures des fluctuations du fond infrarouge, qui seront présentées au chapitre suivant.

---

[5]Pour la petite histoire, Gaelen Marsden et moi nous sommes rendu compte que nous travaillions tous les deux sur le même type de modèle un mois avant de soumettre nos articles. Nous nous sommes mis d'accord pour poster le même jour le papier sur astro-ph.

6.6 Article : *Modeling the evolution of the infrared galaxies : a backward evolution model.*

Mon travail de modélisation, resumé dans ce chapitre, a donné lieu à la publication dans le journal *Astronomy&Astrophysics*.

Astronomy & Astrophysics

Modeling the evolution of infrared galaxies: a parametric backward evolution model

M. Béthermin[1,2], H. Dole[1,2], G. Lagache[1,2], D. Le Borgne[3], and A. Penin[1,2]

Univ Paris-Sud, Laboratoire IAS, UMR8617, 91405 Orsay Cedex, France
e-mail: matthieu.bethermin@ias.u-psud.fr
CNRS, Orsay, 91405
Institut d'Astrophysique de Paris (IAP), UMR 7095 CNRS, UPMC, 98 bis boulevard Arago, 75014 Paris, France

ABSTRACT

Aims. We attempt to model the infrared galaxy evolution in as simple a way as possible and reproduce statistical properties such as the number counts between 15 μm and 1.1 mm, the luminosity functions, and the redshift distributions. We then use the fitted model to interpret observations from *Spitzer*, AKARI, BLAST, LABOCA, AzTEC, SPT, and *Herschel*, and make predictions for *Planck* and future experiments such as CCAT or SPICA.
Methods. This model uses an evolution in density and luminosity of the luminosity function parametrized by broken power-laws with two breaks at redshift ~0.9 and 2, and contains the two populations of the Lagache model: normal and starburst galaxies. We also take into account the effect of the strong lensing of high-redshift sub-millimeter galaxies. This effect is significant in the sub-mm and mm range near 50 mJy. It has 13 free parameters and eight additional calibration parameters. We fit the parameters to the IRAS, *Spitzer*, *Herschel*, and *AzTEC* measurements with a Monte Carlo Markov chain.
Results. The model adjusted to deep counts at key wavelengths reproduces the counts from mid-infrared to millimeter wavelengths, as well as the mid-infrared luminosity functions. We discuss the contribution to both the cosmic infrared background (CIB) and the infrared luminosity density of the different populations. We also estimate the effect of the lensing on the number counts, and discuss the discovery by the South Pole Telescope (SPT) of a very bright population lying at high redshift. We predict the contribution of the lensed sources to the *Planck* number counts, the confusion level for future missions using a $P(D)$ formalism, and the Universe opacity to TeV photons caused by the CIB. Material of the model (software, tables and predictions) is available online[*].

Key words. diffuse radiation – galaxies: statistics – galaxies: evolution – galaxies: star formation – infrared: galaxies – submillimeter: galaxies

1. Introduction

The extragalactic background light (EBL) is the relic emission from galaxy formation and accretion processes since the recombination. The infrared (8 μm < λ < 1000 μm) part of this emission called the cosmic infrared background (CIB) was detected for the first time by Puget et al. (1996) and contains about half of the energy of the EBL (Dole et al. 2006; Béthermin et al. 2010a). Nevertheless, in the local universe, the optical/UV emissions is three times brighter than infrared/sub-millimeter ones (Soifer & Neugebauer 1991; Driver et al. 2008). This pseudo-paradox is explained by a strong evolution in the infrared galaxy properties.

The infrared luminosity density is dominated by normal galaxies ($L_{\rm IR,bolometric} < 10^{11} L_\odot$) in the local Universe (Saunders et al. 1990). At higher redshift, it is dominated by luminous infrared galaxies (LIRG, $10^{11} L_\odot < L_{\rm IR,bolometric} < 10^{12} L_\odot$) at $z = 1$ (Le Floc'h et al. 2005) and ultra-luminous infrared galaxies (ULIRG, $10^{12} L_\odot < L_{\rm IR,bolometric} < 10^{13} L_\odot$) at $z = 2$ (Caputi et al. 2007). The infrared luminosity of these galaxies is correlated to the star formation rate (Kennicutt 1998). Thus, modeling this rapid evolution of the infrared galaxies is very important to understand the history of the star formation.

The physical models (such as Lacey et al. 2010; Wilman et al. 2010; Younger & Hopkins 2011, for the latest) use a physical approach based on semi-analytical recipes and dark matter numerical simulations. They use a limited set of physical parameters, but nowadays they poorly reproduce some basic observational constraints such as the infrared-galaxy number counts (Oliver et al. 2010).

The backward evolution models (like Lagache et al. 2004; Franceschini et al. 2010; Rowan-Robinson 2009; Valiante et al. 2009) use an evolution the luminosity function (LF) of the galaxies to reproduce empirically the galaxy counts, and other constraints. These models describe only the evolution and contain little physics. The parameters of these models were tuned manually to fit observational constraints. Le Borgne et al. (2009) used another approach and performed a non-parametric inversion of the counts to determine the LF. Nevertheless, this approach is complex, uses only one population of galaxy, and does not manage to reproduce the 160 μm number counts. An other fully-empirical approach was used by Domínguez et al. (2011). They fitted the SED from UV to mid-infrared of detected galaxies and extrapolated the far-infrared spectral energy distribution of these galaxies and the contribution of faint populations. Nevertheless, their model aims only to reproduce the CIB, although its ability to reproduce other constraints such as the number counts has not been tested.

---

[*] http://www.ias.u-psud.fr/irgalaxies/

The Balloon-borne Large-Aperture Submillimeter Telescope (BLAST) experiment (Pascale et al. 2008; Devlin et al. 2009) and the spectral and photometric imaging receiver (SPIRE) instrument (Griffin et al. 2010) onboard the *Herschel* space telescope (Pilbratt et al. 2010) performed recently new observations in the sub-mm at 250, 350, and 500 μm. In their current version, most of the models fail to reproduce the number counts measured at these wavelengths (Patanchon et al. 2009; Béthermin et al. 2010b; Clements et al. 2010; Oliver et al. 2010). The Valiante et al. (2009) model gives the best results, using a Monte Carlo approach (sources are randomly taken in libraries) to simulate the temperature scatter and the heterogeneity of the active galactic nucleus (AGN) populations, but this model strongly disagrees with the recent measurements of the redshift distribution of the CIB by Jauzac et al. (2011). It is thus necessary to develop new models that reproduce the recent far-infrared and sub-mm observations.

The discovery of very bright and high-redshift dusty galaxies by Vieira et al. (2010) with the South Pole Telescope (SPT) suggests that the contribution of high-redshift galaxies strongly lensed by dark matter halos of massive low-redshift galaxies on the bright sub-millimeter and millimeter counts is non-negligible. This contribution was discussed by Negrello et al. (2007) and observational evidence of this phenomenon was found by Negrello et al. (2010). We can also cite the simplified approach of Lima et al. (2010), who reproduced the AzTEC and SPT counts using a single population of galaxies with a Schechter LF at a single redshift and a lensing model. We can also cite Hezaveh & Holder (2010) on the effect of the lensing on the SPT counts, based on an advanced lensing model.

We present a new simple and parametric model based on Lagache et al. (2004) SED libraries, which reproduces the new observational constraints. The parameters of this model (13 free parameters and eight calibration parameters) were fitted from a large set of recent observations using a Monte Carlo Markov chain (MCMC) method, allowing us to study degeneracies between the parameters. This model also includes the effects of the strong lensing on the observations. We make predictions about the confusion limit for future missions, the high-energy opacity of the Universe, and the effects of strong lensing on the counts. This model is plugged into a halo model to study the spatial distribution of the infrared galaxies in a companion paper (Penin et al., in prep.). We note that another study also using MCMC methods was performed by Marsden et al. (2011) at the same time as ours.

We use the WMAP seven-years best-fit ΛCDM cosmology model (Larson et al. 2011) in this paper. We thus assume that $H_0 = 71$ km s^{-1} Mpc^{-1}, $\Omega_\Lambda = 0.734$, and $\Omega_m = 0.266$.

2. Approach

The backward evolution models are not based on physical parameters. Each model uses different evolving populations to reproduce the observational constraints. Some models (such as Franceschini et al. 2010; Rowan-Robinson 2009) use four galaxy populations evolving separately to reproduce the observations. Valiante et al. (2009) take randomly galaxy SEDs from a very large library of templates and claim that the contribution of the AGNs and the dispersion in the dust temperature of the galaxies must be taken into account to reproduce the observational constraints. Our approach is to keep the model as simple as possible, but to use advanced methods to constrain its free parameters. This new parametric model can be used as an input for halo modeling or $P(D)$ analysis for instance.

As we show, we need neither an AGN contribution nor a temperature dispersion to reproduce the current observational constraints. In the local Universe, the AGNs only dominate in the ULIRG regime (Imanishi 2009). Alexander et al. (2005) estimate an AGN contribution of 8% to the submillimeter galaxies (SMG). Fadda et al. (2010) showed that the proportion of AGN-dominated sources is rather small for LIRGs at $z \sim 1$ (5%) and ULIRGs around $z \sim 2$ (12%). Jauzac et al. (2011) demonstrated that the AGN contribution to the CIB is less than 10% at $z < 1.5$. These categories of luminosity dominate the infrared output at their redshift. The small contribution of AGNs to these categories explains why AGNs are not necessary to reproduce the mean statistical properties of the galaxies. Nevertheless, despite their small contribution to the infrared output, the AGNs play a central role in the physics of galaxies.

Our model takes into account the strong lensing of high redshift galaxies by the dark matter halos of elliptical galaxies. According to the results of Sect. 7.3, the effect of the lensing on the counts we fitted is smaller than 10%. The model of lensing does not have free parameters. It is based on the WMAP seven-years best-fit cosmology and on some parameters taken at values given by the litterature. The lensing is thus not useful to reproduce the current observations, but is necessary to make predictions at bright fluxes (>100 mJy) in the sub-mm and mm range, where the effects of the lensing are large.

3. Description of the model

3.1. Basic formulae

The flux density S_ν at a frequency ν of a source lying at a redshift z is (Hogg 1999) is

$$S_\nu = \frac{(1+z)L_{(1+z)\nu}}{4\pi D_L^2(z)},\tag{1}$$

where z is the redshift, D_L is the luminosity distance of the source, and $L_{(1+z)\nu}$ is the luminosity at a frequency $(1+z)\nu$. The comoving volume corresponding to a redshift slice between z and $z + dz$ and a unit solid angle is

$$\frac{dV}{dz} = D_H \frac{(1+z)^2 D_A^2}{\sqrt{\Omega_\Lambda + (1+z)^3 \Omega_m}},\tag{2}$$

where D_H is the Hubble distance ($D_H = c/H_0$), D_A the angular distance to the redshift z, and Ω_m and Ω_Λ are the normalized energy density of the matter and the cosmological constant, respectively.

3.2. Bolometric luminosity function and its evolution

We assume that the luminosity function (LF) is a classical double-exponential function (Saunders et al. 1990)

$$\Phi(L_{IR}) = \Phi^\star \times \left(\frac{L_{IR}}{L^\star}\right)^{1-\alpha} \times \exp\left[-\frac{1}{2\sigma^2}\log_{10}^2\left(1 + \frac{L_{IR}}{L^\star}\right)\right],\tag{3}$$

where $\Phi(L_{IR})$ is the number of sources per logarithm of luminosity and per comoving volume unit for an infrared bolometric luminosity L_{IR}, $\Phi_\star$ is the normalization constant characterizing the density of sources, $L_\star$ is the characteristic luminosity at the break, and $1 - \alpha$ and $1 - \alpha - 1/\sigma^2/\ln^2(10)$ are the slope of the asymptotic power-law behavior at, respectively, low and high luminosity.
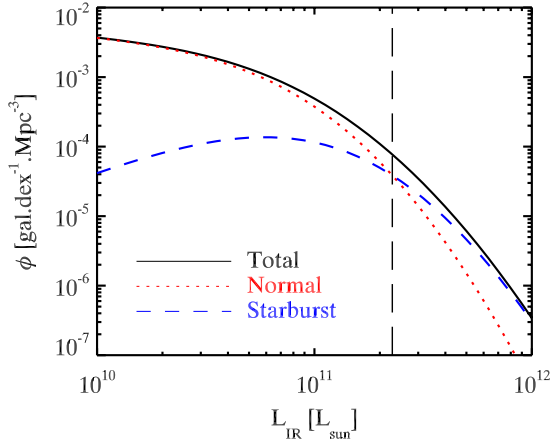
Fig. 1. Solid line: local infrared bolometric luminosity function from our best-fit model. Red dotted line: contribution of the normal galaxies. Blue dashed line: contribution of the starburst galaxies. Black vertical long dashed line: luminosity of the transition between the two population (L_{pop}).

We assume a continuous evolution in luminosity and density of the luminosity function with the redshift of the form $L^{\star} \propto (1 + z)^{r_L}$ and $\Phi^{\star} \propto (1 + z)^{r_\Phi}$, where r_L and r_ϕ are coefficients driving the evolution in luminosity and density, respectively. It is impossible to reproduce the evolution of the LF with constant r_L and r_ϕ. We consequently authorize their value to change at some specific redshifts. The position of these breaks are the same for both r_L and r_ϕ. The position of the first redshift break is a free parameter and converges to the same final value for initial values between 0 and 2. To avoid a divergence at high redshift, we also add a second break fixed at $z = 2$.

3.3. Spectral energy distribution (SED) of the galaxies

We use the Lagache et al. (2004) SED library. This library contains two populations: a starburst and a normal one. This library is parametrized only by the infrared bolometric luminosity (L_{IR}). There is no evolution of the SED with redshift. The normal population has that is a spectrum typical of a spiral galaxy. The SED of this population does not evolve with L_{IR}. In contrast, the starburst SED evolves with L_{IR}. The brighter the starburst galaxy, the hotter the dust.

The normal galaxies are dominant at low luminosity and the starburst at high luminosity. We thus chose arbitrarily a smooth function to describe the fraction of starburst galaxies as a function of the bolometric luminosity L_{IR}

$$\frac{\Phi_{\text{starburst}}}{\Phi} = \frac{1 + \text{th}[\log_{10}(L_{IR}/L_{pop})/\sigma_{pop}]}{2}, \quad (4)$$

where th is the hyperbolic tangent function, L_{pop} is the luminosity at which the number of normal and starburst galaxies are equal, and σ_{pop} characterizes the width of the transition between the two populations. At $L_{IR} = L_{pop}$, the fraction of starbursts is 50%. The fraction of starbursts is 88% at $L_{IR} = L_{pop} \times 10^{\sigma_{pop}}$, and 12% at $L_{IR} = L_{pop} \times 10^{-\sigma_{pop}}$. The contribution of the different populations to the local infrared bolometric LF is shown in Fig. 1.

3.4. Observables

The number counts at different wavelengths are an essential constraint of our model. The source extraction biases are in general accurately corrected for these observables. The counts are computed with the formula

$$\frac{dN}{dS_\nu d\Omega}(S_\nu) = \sum_{\text{pop}} \int_0^\infty f_{\text{pop}}(L_{IR}) \frac{dN}{dL_{IR} dV}\Big|_{L_{IR}(S_\nu, z, \text{pop})} \frac{dL_{IR}}{dS_\nu} \frac{dV}{dz d\Omega} dz$$

$$= \sum_{\text{pop}} \int_0^\infty \frac{dN}{dS_\nu dz d\Omega} dz, \quad (5)$$

where $dN/dS_\nu/d\Omega$ is the number of source per flux unit and per solid angle, $f_{\text{pop}}(L_{IR})$ is the fraction of the sources of a given galaxy population computed with Eq. (4), and $dN/dL_{IR}/dV$ is computed from Eq. (3) to be

$$\frac{dN}{dL_{IR} dV} = \frac{dN}{d\log_{10}(L_{IR}) L_{IR} \log(10) dV} = \frac{\Phi(L_{IR})}{L_{IR} \log(10)}, \quad (6)$$

where $L_{IR}(S_\nu, z, \text{pop})$ and dL_{IR}/dS_ν were computed on a grid in S_ν and z from the cosmology and the SED templates. These grids depend on neither the evolution of the LF nor the population mixing parameters. These grids are thus generated only once and saved to accelerate the computation of the counts. We note that with this method, it is very easy to change the SED templates and/or add other populations.

Other measurements help us to constrain our model. For example, the monochromatic luminosity Φ_{mono} function at a given redshift is

$$\Phi_{\text{mono}} = \sum_{\text{pop}} f_{\text{pop}}(L_{IR}(\nu L_\nu)) \phi(L_{IR}(\nu L_\nu)) \frac{d\log_{10}(L_{IR})}{d(\nu L_\nu)}. \quad (7)$$

We do not use the bolometric LFs, because they are biased by the choice of the assumed SED of the sources.

We can also compute the redshift distribution $N(z)$ for a selection in terms of flux $S_\nu > S_{\nu,\text{cut}}$ with

$$N(z, S_{\text{cut}}) = \int_{S_{\nu,\text{cut}}}^\infty \frac{dN}{dS_\nu dz} dS_\nu. \quad (8)$$

The extragalactic background due to the galaxies at a given wavelength is

$$B_\nu = \int_{z=0}^\infty \int_{S_\nu=0}^\infty S_\nu \frac{dN}{dS_\nu dz d\Omega} dS_\nu\, dz = \int_{S_\nu=0}^\infty S_\nu \frac{dN}{dS_\nu d\Omega} dS_\nu, \quad (9)$$

and can be compared to the measurements of the CIB.

The level of the non-correlated fluctuations (shot-noise) of the CIB can be easily computed from our model with the equation

$$P_{\text{SN}} = \int_0^{S_{\nu,\text{cut}}} S_\nu^2 \frac{dN}{dS_\nu d\Omega} dS_\nu, \quad (10)$$

where P_{SN} is the level of the non-correlated fluctuations and $S_{\nu,\text{cut}}$ the flux limit for the cleaning of the resolved sources.

3.5. Effect of the strong lensing on the counts

We use a simple strong-lensing model based on Perrotta et al. (2001, 2002), which assumes that the dark matter halos are singular isothermal spheres. The cross-section σ of a halo for a magnification μ larger than μ_{min} is

$$\sigma(\mu > \mu_{\text{min}}) = \frac{4\pi \alpha^2 D_{A,ls}}{\mu^2}, \quad (11)$$

where $D_{A,ls}$ is the angular-diameter distance between the lens and the source and α is given by

$$\alpha = 4\pi \frac{\sigma_v^2}{c^2}, \tag{12}$$

where c is the speed of light and σ_v the velocity dispersion in the halo, which depends on the cosmology, the redshift, and the mass of the halo.

The probability $P(\mu_{min}, z_s)$ that a source at a redshift z_s is magnified by a factor greater than μ_{min} is

$$P(\mu > \mu_{min}, z_s) = \frac{(1+z_s)^2}{4\pi D_c(z_s)} \int_0^{z_s} \int_0^\infty \frac{dN}{d(\log_{10}(M))\,dV}$$
$$\times \sigma(\mu > \mu_{min}) \frac{dV}{dz} dM dz, \tag{13}$$

where z_s is the redshift of the source, D_c the comoving radial distance, $\frac{dN}{d(\log_{10}(M))\,dV}$ is the halo mass function, and $\frac{dV}{dz}$ is the comoving volume associated with the redshift slice dz. We use the halo mass function of Reed et al. (2007).

The counts derived by our model take into account the fact that a small fraction of the sources are gravitationally magnified, i.e., the observed number counts taking into account the lensing $(dN/dS_\nu/d\Omega)_{lensed}$ are computed from initial counts $dS_\nu/dz/d\Omega$ with

$$\left(\frac{dN}{dS_\nu d\Omega}\right)_{lensed}(S_\nu) = \int_0^\infty \int_{\mu_{min}}^{\mu_{max}} \frac{dP}{d\mu}(z) \frac{1}{\mu} \frac{dN}{dS_\nu dz d\Omega}\left(\frac{S_\nu}{\mu}, z\right) d\mu\, dz. \tag{14}$$

In practice, this operation is performed by multiplying the vector containing the counts for a given redshift slice by a matrix describing the effects of lensing. This lensing matrix has diagonal coefficients values of around 1, and small ($<10^{-3}$) non-diagonal terms. These non-diagonal terms describe how the magnified faint sources affect the counts at brighter fluxes. The effect of the lensing on the monochromatic luminosity function was computed in the same way. We chose $\mu_{min} = 2$, which corresponds to the limit of the validity of the strong-lensing hypothesis (Perrotta et al. 2001). The spatial extension of the lensed galaxies limits the maximum magnification. According to Perrotta et al. (2002), μ_{max} is in the range 10–30. We chose to use $\mu_{max} = 20$ in this paper. Negrello et al. (2007) used $\mu_{min} = 2$ and $\mu_{max} = 15$.

Figure 2 illustrates how number counts are affected by lensing. This figure is based on the number counts predicted by the model at $850\,\mu m$ where the probability of magnification has been multiplied by a factor 10 to enhance the effect. The green dashed line represents contribution of the lensed sources. Owing to the magnification, the peak of this contribution is at higher flux than for non-lensed sources, and because of the small probability of lensing, the peak is lower than for non-lensed sources. This effect of the magnification on the counts become non-negligible when the slope of the counts is very steep, as in the sub-mm and mm domain.

4. Fitting the model parameters to the data

Our model has several free parameters. We attempted to use the minimum number of free parameters, which were determined by fitting the model to published measurements of the counts and LFs. We used a Monte Carlo Markov chain (MCMC) to identify the best-fit parameters, their uncertainties, and their degeneracies. We do not fit the measured redshift distributions, because the cosmic variance and the selection effects are currently not accurately enough known.
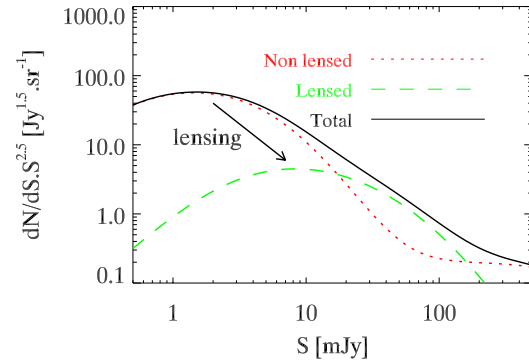
Fig. 2. Effect of the lensing on the number counts at 850 microns. The contribution of lensed sources is multiplied by ten to underline the effect of the lensing on the counts. Red dotted line: counts of non-lensed sources. Green dashed line: counts of lensed sources. Black solid line: total counts.

4.1. Data: extragalactic number counts

4.1.1. Data used for the fit

We chose to fit the following data:

- *Spitzer* MIPS counts of Béthermin et al. (2010a) at 24, 70, and 160 μm;
- *Herschel* SPIRE Oliver et al. (2010) counts at 250, 350, and 500 μm;
- AzTEC counts of Austermann et al. (2010) and Scott et al. (2010) at 1.1 mm.

4.1.2. Justification of our choice

We fit only the differential number counts since the integral counts are highly correlated and the correlation matrix is rarely estimated.

The number counts were measured at numerous bands between 15 μm and 1.1 mm. We chose a collection of points. We were guided by the reliability of the measurements and their error bars.

Number counts at 15 μm based on Infrared Space Observatory (ISO) data (Elbaz et al. 1999; Gruppioni et al. 2002) and the AKARI data (Pearson et al. 2010; Hopwood et al. 2010) differ by a factor of about 2, and their errors do not include the effects of cosmic variance. The results of these papers were not used for the fit. Nevertheless, we compared a posteriori these measurements to our own results to check for consistency in Sect. 5.4.

We fitted the *Spitzer* MIPS counts of Béthermin et al. (2010a) at 24, 70, and 160 μm. These points were measured from the data of FIDEL, COSMOS, and SWIRE legacy programs. The errors bars take into account the cosmic variance. These counts agree with the previous *Spitzer* measurements of Papovich et al. (2004), Shupe et al. (2008), Le Floc'h et al. (2009), and Frayer et al. (2009) and *Herschel* measurements of Berta et al. (2010) (in which the different fields were not combined).

At 250 μm, 350 μm, and 500 μm, we fitted the *Herschel* SPIRE counts of Oliver et al. (2010) which take into account the cosmic variance and the deboosting uncertainty. These counts agree with the BLAST measurements of Patanchon et al. (2009)

and Béthermin et al. (2010b) and the *Herschel* measurements of Clements et al. (2010). We chose Oliver et al. (2010) counts because *Herschel* data are points more accurate than BLAST ones and because Clements et al. (2010) counts use only Poissonian error bars, which could be largely underestimated. For instance, Béthermin et al. (2010a) estimate that the Poissonian uncertainties underestimate the real sample uncertainties by a factor three for counts around 100 mJy at 160 μm in a 10 deg^2 field.

We do not fit the 850 μm because of the large discrepancies between the Submillimeter Common-User Bolometer Array (SCUBA) observations (Coppin et al. 2006) and the Large APEX BOlometer CAmera (LABOCA) observations (Weiß et al. 2009). We discuss this problem in the Sect. 5.4.

We fitted the AzTEC measurements at 1.1 mm of Austermann et al. (2010) and Scott et al. (2010). The area covered by AzTEC is small compared to that covered by *Spitzer* and *Herschel*. We used two independent measurements of the AzTEC counts to increase the weight of the mm observations in our fit.

4.2. Data: monochromatic luminosity functions

4.2.1. Data used for the fit

We chose to fit the following data:

– InfraRed Astronomical Satellite (IRAS) local luminosity function at 60 μm of Saunders et al. (1990);
– *Spitzer* local luminosity function at 24 μm of Rodighiero et al. (2010);
– *Spitzer* luminosity function at 15 μm at $z = 0.6$ of Rodighiero et al. (2010);
– *Spitzer* luminosity function at 12 μm at $z = 1$ of Rodighiero et al. (2010);
– *Spitzer* luminosity function at 8 μm at $z = 2$ of Caputi et al. (2007).

4.2.2. Justification of our choice

We fitted some monochromatic luminosity functions. We chose only wavelengths and redshifts for which no K-corrections are needed. These observations strongly constrain the parameters driving the redshift evolutions of our model.

From the Rodighiero et al. (2010) LFs measured with the *Spitzer* data at 24 μm, we computed three non K-corrected LFs at $z = 0$, 0.6, and 1. We used their local LF at 24 μm. At $z = 0.6$ and 1, instead of directly using their results in their redshift bins, we combined their 15 μm LF at $z = 0.6$ (respectively, 12 μm LF at $z = 1$) in the $0.45 < z < 0.6$ and $0.6 < z < 0.8$ bins (respectively, $0.8 < z < 1.0$ and $1.0 < z < 1.4$) to obtain our version of the 15 μm LF at $z = 0.6$ (respectively, 12 μm LF at $z = 1$). The error in a point is the maximum of the combined statistical errors of the two bins and the difference between the measurements in the two bins. The second value is often larger because of the rapid evolution of the LF and the cosmic variance. We fitted only the points that do not suffer incompleteness to avoid possible biases. We also fitted the 8 μm at $z = 2$ of Caputi et al. (2007).

We also fitted the local LF at 60 μm determined from IRAS data (Saunders et al. 1990) to better constrain the faint-end slope of the local LF. Owing to the strong AGN contamination at 60 μm in the ULIRG regime, we did not fit the points brighter than $10^{11.5} L_\odot$ at 60 μm.

4.3. Data: CIB

The bulk of the CIB is not resolved at SPIRE wavelengths. We thus used the absolute measurement of the CIB level in SPIRE bands as a constraint of our model. We used the Lagache et al. (1999) measurement derived from the far-infrared absolute spectrophotometer (FIRAS) data: 11.7 ± 2.9 nW m^2 sr^{-1} at 250 μm, 6.4 ± 1.6 nW m^2 sr^{-1} at 350 μm, and 2.7 ± 0.7 nW m^2 sr^{-1} at 500 μm. We assume that the CIB is only due to galaxies, thus neglect any possible extragalactic diffuse emission.

4.4. Calibration uncertainties

The calibration uncertainty is responsible for correlated uncertainties between points measured at a given wavelength with the same instrument. A change in the calibration globally modifies both the number counts and the LF. Assuming that the "good" calibration is obtained by multiplying the fluxes by a factor γ, the "good" normalized counts are obtained with $S_{\text{new}} = \gamma S$ and $(S_{\text{good}}^{2.5} dN/dS_{\text{good}}) = \gamma^{1.5} (S^{2.5} dN/dS)$. The effect on the LF in dex per volume unit is more simple. We just have to shift the luminosity in abscissa by a factor γ.

To our free parameters, we added a calibration parameter for each fitted band (see Table 2). We took into account the uncertainties in the calibration estimated by the instrumental team, in our fit (Stansberry et al. 2007; Gordon et al. 2007; Engelbracht et al. 2007; Swinyard et al. 2010; Scott et al. 2010).

4.5. Fitting method

To fit our points, we assumed that the uncertainties in both the measurements and calibrations are Gaussian and uncorrelated. The log-likelihood is then

$$-\log(L(\theta)) = \sum_{k=1}^{N\text{points}} \frac{(m_k - m_{\text{model},k}(\theta))^2}{2\sigma_m^2} + \sum_{b=1}^{N\text{band}} \frac{(\gamma_b - 1)^2}{2\sigma_{\text{calib},b}^2}, \quad (15)$$

where L is the likelihood, θ the parameters of the model, m_k a measurement, $m_{\text{model},k}$ the prediction of the model for the same measurement, σ_m the measurement uncertainty on it, γ_b the calibration parameter of the band b, and $\sigma_{\text{calib},b}$ the calibration uncertainty for this band.

We used a Monte Carlo Markov chain (MCMC) Metropolis-Hastings algorithm (Chib & Greenberg 1995; Dunkley et al. 2005) to fit our model. The method consists of a random walk in the parameter space. At each step, a random shift of the parameters is performed using a given fixed proposal density. The new step n is accepted with a probability of 1 if $L(\theta_n) > L(\theta_{n-1})$ or otherwise a probability $L(\theta_n)/L(\theta_{n-1})$. The distribution of the realization of the chain is asymptotically the same as the underlying probability density. This property is thus very convenient to determine the confidence area of the model parameters.

We used the Fisher matrix formalism to determine the proposal density of the chain from initial parameters values that had been set manually. The associated Fisher matrix is

$$F_{ij}(\theta) = \sum_{k=1}^{N\text{point}} \frac{\partial m_{\text{model},k}}{\partial \theta_i} \frac{\partial m_{\text{model},k}}{\partial \theta_j} \frac{1}{2\sigma_m^2} \left(+ \frac{1}{2\sigma_{\text{calib},b}^2} \right), \quad (16)$$

where θ is a vector containing the model and calibration (γ_b) parameters. The term in brackets appears only for the diagonal terms corresponding to a calibration parameter. We performed a first short chain (10 000 steps) and computed a new proposal
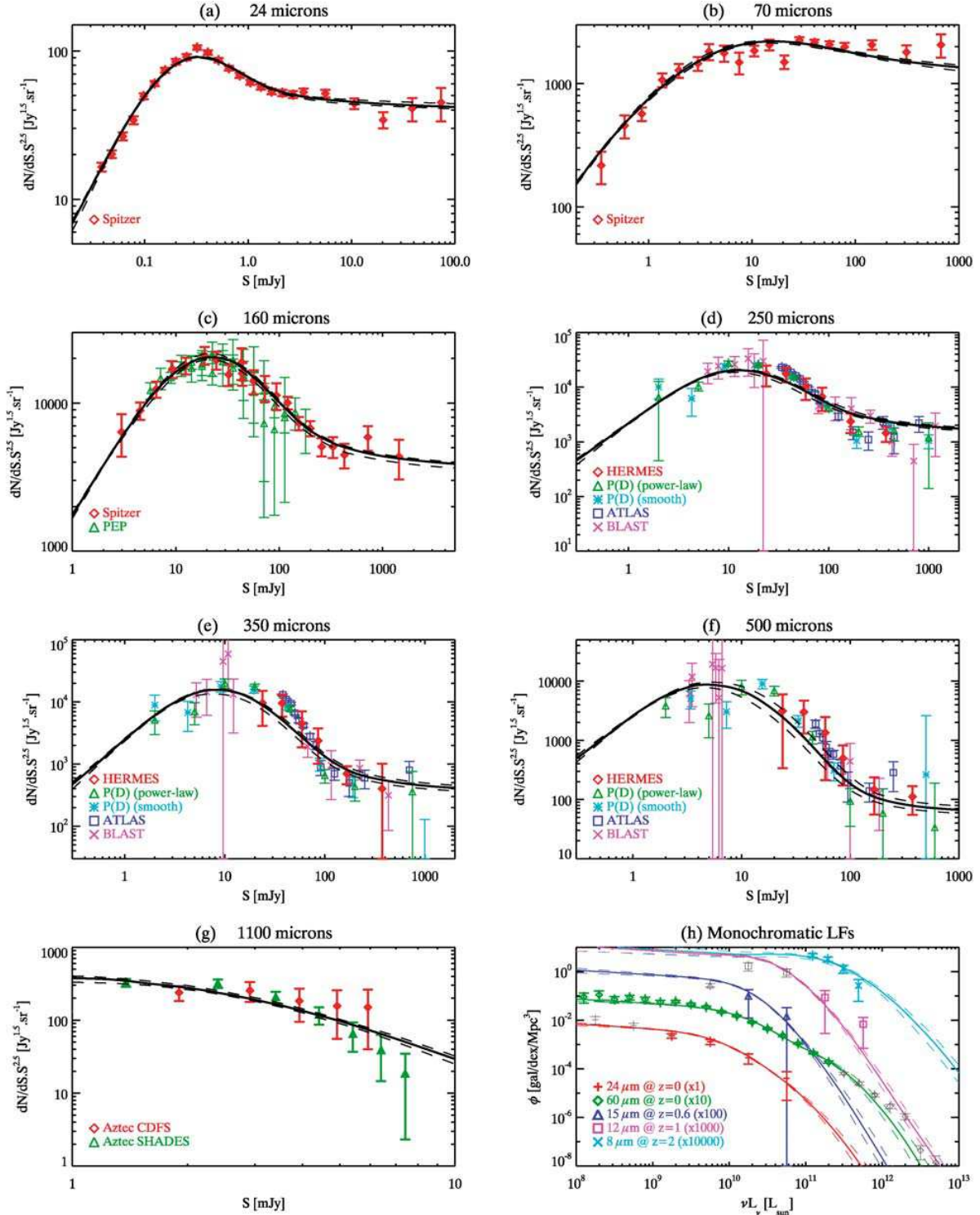
Fig. 3. **a)**–**f)** Differential extragalactic number counts used for the fit. **h)** Monochromatic LFs at different wavelengths and redshifts. **a)**–**h)** The fitted points are thicker. Black solid line: our best-fit model. Black dashed line: 1-σ range of the model. **a)**–**c)** Red diamonds: Béthermin et al. (2010a) *Spitzer* legacy number counts. **c)** Green triangles: Berta et al. (2010) *Herschel*/PEP number counts. **d)**–**f)** Red diamonds: Oliver et al. (2010) *Herschel*/Hermes number counts. Green triangles: Glenn et al. (2010) *Herschel*/Hermes $P(D)$ analysis. Clements et al. (2010) *Herschel*/ATLAS number counts. Purple cross: Béthermin et al. (2010b) BLAST number counts. **g)** Green triangles: Scott et al. (2010) AzTEC number counts in the CDFS field. Green triangles: Austermann et al. (2010) AzTEC number counts in the SHADES field. **h)** Red plus: Rodighiero et al. (2010) local 24 μm LF (not fitted points in grey). Green diamonds: Saunders et al. (1990) local 60 μm LF (shifted by a factor 10 on the *y*-axis; not fitted points in grey); blue triangles: Rodighiero et al. (2010) 15 μm LF at $z = 0.6$ (shifted by a factor 100 on the *y*-axis; not fitted points in grey). Purple squares: Rodighiero et al. (2010) 12 μm LF at $z = 1$ (shifted by a factor 1000 on the *y*-axis; not fitted points in grey). Cyan crosses: Caputi et al. (2007) 8 μm LF at $z = 2$ (shifted by a factor 10 000 on the *y*-axis).

Table 1. Parameters of our model fitted to our selection of infrared observations.

Parameter	Description	Value
α	Faint-end slope of the infrared bolometric LF	1.223 ± 0.044
σ	Parameter driving the bright-end slope of the LF	0.406 ± 0.019
$L_\star(z=0)$ ($\times 10^{10}\,L_\odot$)	Local characteristic luminosity of the LF	2.377 ± 0.363
$\phi_\star\,(z=0)$ ($\times 10^{-3}$ gal/dex/Mpc^3)	Local characteristic density of the LF	3.234 ± 0.266
$r_{L_\star,lz}$	Evolution of the characteristic luminosity between 0 and $z_{\mathrm{break},1}$	2.931 ± 0.119
$r_{\mathrm{phi}_\star,lz}$	Evolution of the characteristic density between 0 and $z_{\mathrm{break},1}$	0.774 ± 0.196
$z_{\mathrm{break},1}$	Redshift of the first break	0.879 ± 0.052
$r_{L_\star,mz}$	Evolution of the characteristic luminosity between $z_{\mathrm{break},1}$ and $z_{\mathrm{break},2}$	4.737 ± 0.301
$r_{\mathrm{phi}_\star,mz}$	Evolution of the characteristic density of between $z_{\mathrm{break},1}$ and $z_{\mathrm{break},2}$	-6.246 ± 0.458
$z_{\mathrm{break},2}$	Redshift of the second break	2.000 (fixed)
$r_{L_\star,hz}$	Evolution of the characteristic luminosity for $z > z_{\mathrm{break},2}$	0.145 ± 0.460
$r_{\mathrm{phi}_\star,hz}$	Evolution of the characteristic density for $z > z_{\mathrm{break},2}$	-0.919 ± 0.651
L_{pop} ($\times 10^{10}\,L_\odot$)	Luminosity of the transition between normal and starburst templates	23.677 ± 2.704
σ_{pop}	Width of the transition between normal and starburst templates	0.572 ± 0.056

Notes. The errors are derived from the MCMC analysis.

Table 2. Calibration parameters and 1-σ marginalized errors from our MCMC fit compared with calibration uncertainties given by the instrumental teams.

Instrument	Calibration parameter (γ_b)	Calib. uncertainty
MIPS 24 μm	1.00 ± 0.03	4%
MIPS 70 μm	1.06 ± 0.04	7%
MIPS 160 μm	0.96 ± 0.03	12%
SPIRE 250 μm	0.88 ± 0.05	15%
SPIRE 350 μm	0.97 ± 0.07	15%
SPIRE 500 μm	1.17 ± 0.1	15%
AzTEC 1.1 mm	0.98 ± 0.09	9%

density with the covariance matrix of the results. We then executed a second long chain of 300 000 steps. The final chain satisfies the Dunkley et al. (2005) criteria ($j^\star > 20$ and $r < 0.01$).

5. Results of the fit

5.1. Quality of the fit

Our final best-fit model has a χ^2 ($\chi^2 = -2\log(L)$ because all errors are assumed to be Gaussian) of 177 for 113 degrees of freedom. Our fit is thus reasonably good. The parameters found with the fit are given in Table 1 (the uncertainties are computed from the MCMC). The calibration factor are compatible with the calibration uncertainties given by the instrumental teams with a χ^2 of 2.89 for seven points (see Table 2). The results are plotted in Fig. 3.

5.2. Comparison between the model and the observed counts used in the fit

The Béthermin et al. (2010a) points fit globally well, with some exceptions. Our model is lower by about 15% than two points around 300 μJy at 24 μm. These two points where produced combining data for the FIDEL, COSMOS and SWIRE fields. The SWIRE fields are shallow fields and the counts could be affected by the Eddington bias. We also observe a slight underprediction of the bright ($S_{70} > 50$ mJy) counts at 70 μm. We also plotted the Berta et al. (2010) counts at 160 μm measured using the photodetector array camera and spectrometer (PACS) on the *Herschel* satellite. These counts agree with Béthermin et al. (2010a) and our model.

Our model fits globally well the Oliver et al. (2010) and Béthermin et al. (2010b) counts, apart from a slight underprediction of the counts between 30 mJy and 100 mJy at 500 μm. There is a mild disagreement with the Clements et al. (2010) counts, but their errors bars do not take into account the cosmic variance and are thus underestimated. We also plotted the results of the $P(D)$ analysis of Glenn et al. (2010). These points and especially the error bars must be interpreted with caution (see the complete discussion in Glenn et al. 2010). We have plotted the knots of the smooth and power-law models, which globally agree with our model.

Our model agrees very well with the AzTEC counts of Austermann et al. (2010) and Scott et al. (2010). The contribution of the strong lensing objects to the AzTEC counts is weak (<10%, see Sect. 7.3).

5.3. Comparison between the model and the observed monochromatic LFs

Our model closely reproduces our collection of LFs (Saunders et al. 1990; Caputi et al. 2007; Rodighiero et al. 2010), apart from the brightest point of Caputi et al. (2007). In Fig. 3, we arbitrarily shifted the different LFs on the y-axis to obtain a clearer plot. Our model underestimates the 60 μm local LF in the ULIRG regime. It is expected because our model does not contain AGNs and confirms our choice of not fitting these points (Sect. 4.2).

### 5.4. Comparison between the model and the observed counts not used in the fit

We also compared our results with the counts at other wavelengths. They are plotted in Figs. 4 and 5. The 1-σ region of the model includes the γ_b uncertainty of AKARI at 15 μm (4%, Ishihara et al. 2010), PACS at 110 μm (about 10%, Berta et al. 2010), and LABOCA at 850 μm (8.5%, Weiß et al. 2009). The uncertainty in γ_b is about the same for LABOCA and SCUBA (~10%, Scott et al. 2006). The uncertainties in the model are larger at these non-fitted wavelengths because the correlations between the model and the calibration parameters are not taken into account by the fit.

At 15 μm, the Elbaz et al. (1999) counts from different fields are incompatible with each other, but our counts coincide with in the cloud of points. The Gruppioni et al. (2002)

(a) 15 microns

(b) 60 microns

(c) 110 microns
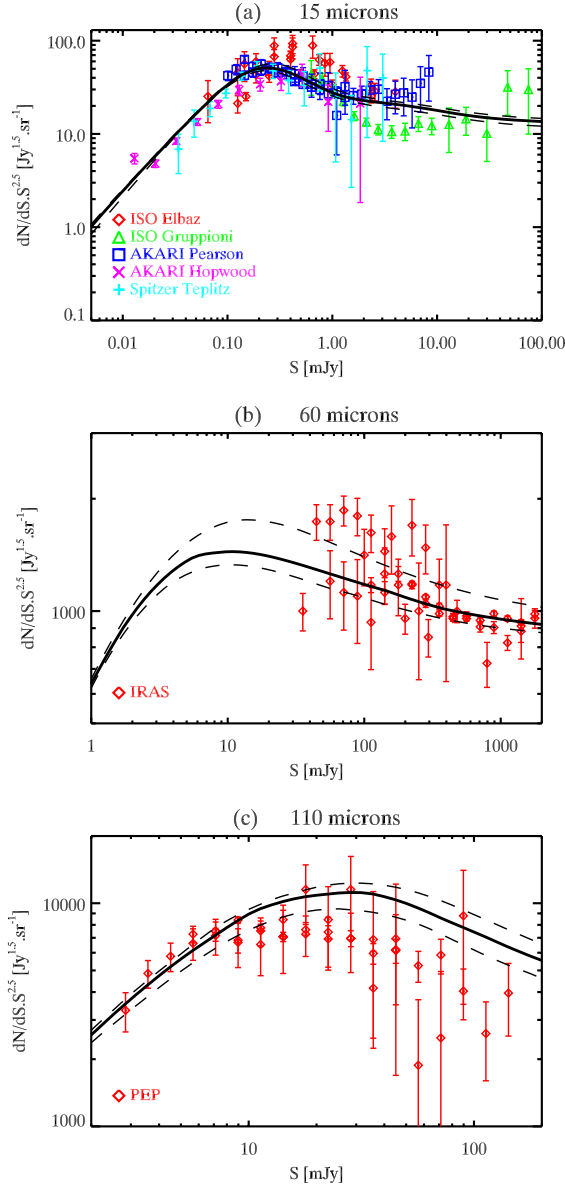
Fig. 4. **a)–c)** Differential extragalactic number counts not used for the fit. Black solid line: our best-fit model. Black dashed line: 1-σ range of the model. **a)** Red diamonds: Elbaz et al. (1999) ISO counts. Green triangle: Gruppioni et al. (2002) ISO counts. Blue squares: Pearson et al. (2010) AKARI counts. Purple cross: Hopwood et al. (2010) AKARI (lensed) counts. Cyan plus: Teplitz et al. (2011) *Spitzer*/IRS counts. **b)** Red diamonds: Hacking & Houck (1987), Lonsdale et al. (1990), Rowan-Robinson et al. (1990), Saunders et al. (1990), Gregorich et al. (1995) and Bertin et al. (1997) IRAS counts. **c)** Red diamonds: Berta et al. (2010) *Herschel*/PEP counts.

counts are significantly lower than our model and other works. We marginally agree with the Pearson et al. (2010) counts. The Hopwood et al. (2010) counts measured with AKARI in a field around Abell 2218 are lower than our model by about 25%. Nevertheless, their field is very narrow and their estimation may be affected by cosmic variance. Finally, we agree with the Teplitz et al. (2011) measurements performed with the infrared spectrograph (IRS) onboard the *Spitzer* space telescope.

850 μm
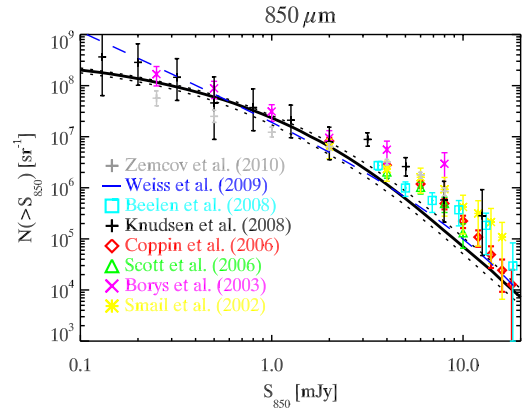
Fig. 5. Integral number counts at 850 μm. Black solid line: our best-fit model. Black dashed line: 1-σ range of the model. Grey plus: Zemcov et al. (2010) combined SCUBA lensed counts. Blue dashed line: Weiß et al. (2009) LABOCA $P(D)$ (Schechter model). Red diamonds: Coppin et al. (2006) SCUBA SHADES counts. Cyan square: (Beelen et al. 2008) LABOCA counts around the J2142-4423 Lyα protocluster. Black plus: Knudsen et al. (2008) combined SCUBA lensed counts; green triangles: Scott et al. (2006) revisited SCUBA counts. Purple cross: Borys et al. (2003) SCUBA HDFN counts. Yellow asterisks: Smail et al. (2002) lensed counts.

We compare our counts to Hacking & Houck (1987), Lonsdale et al. (1990), Rowan-Robinson et al. (1990), Saunders et al. (1990), Gregorich et al. (1995), and Bertin et al. (1997) at 60 μm from IRAS data. There are disagreements between the different observations and some error bars may be underestimated, but our model globally agrees with the cloud of points.

We can also compare the prediction of our model with the Berta et al. (2010) counts at 110 μm. Our model globally agrees with their work, although our model tends to be higher than their measurement near 100 mJy. Observations of several larger fields will help us to see wether this effect is an artifact or not.

At 850 μm, we closely agree with the $P(D)$ analysis of the LABOCA data of Weiß et al. (2009, see Fig. 5). However, the measurements performed with SCUBA (Borys et al. 2003; Scott et al. 2006; Coppin et al. 2006) and LABOCA (Beelen et al. 2008) are significantly higher than our model at 6 and 8 mJy. At low fluxes (<2 mJy), our model agrees very well with the measurement performed in lensed regions (Smail et al. 2002; Knudsen et al. 2008; Zemcov et al. 2010).

We also compare our model predictions with SPT measurements at 1.38 mm (Vieira et al. 2010). At this wavelength, the contribution of the synchrotron emission from the local radio galaxies to the counts is not negligible. Nevertheless, these sources can be separated from dusty galaxies by considering their spectrum. We thus compare our results with the counts of dusty sources. Vieira et al. (2010) measured counts for all the dusty sources and the dusty sources without IRAS 60 μm counterparts. Our model agrees with these two measurements. Figure 6 shows the counts of the non-IRAS dusty sources. The 7.2% calibration uncertainty of SPT is taken into account in the 1-σ region of the model.

5.5. Comparison with the observed redshift distributions

In Fig. 7, we compare our model predictions with observed redshift distributions. At 24 μm, our model overpredicts by about 20% the number of sources below $z = 1$ according to
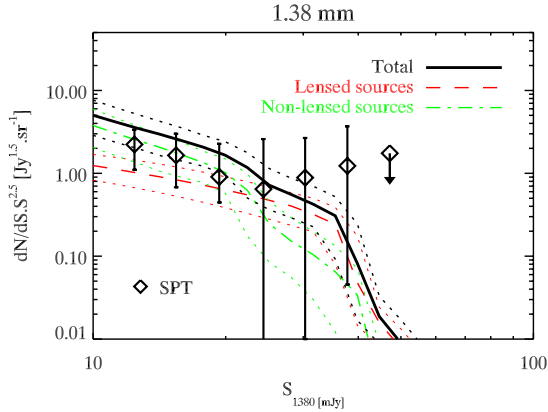
Fig. 6. Number counts at 1.38 mm of dusty sources without IRAS 60 μm counterpart. Black diamonds: Vieira et al. (2010) south pole telescope (SPT) measurements. Black solid line: total contribution of $S_{60} < 0.2$ Jy sources. Green dot-dashed line: contribution of the non-lensed sources. Red dashed line: contribution of the strongly-lensed sources. Dotted lines 1-σ contours.

Le Floc'h et al. (2009) observations for the selection $S_{24} > 80 \mu$Jy. Nevertheless, these authors excluded $i^+_{AB} < 20$ galaxies and their number of sources at low redshift is thus underestimated. Our model also underpredicts the number of sources at $z > 3$. However, the redshifts of the $z > 2$ sources are only moderately accurate ($\sigma_z \approx 0.25$ for $i^+_{AB} > 25$ at $z \sim 2$). Because of the steep slope of the redshift distribution, a significant number of sources measured near $z = 3.5$ could be sources lying around $z = 3$ with overestimated redshifts. If we convolve our model with a Gaussian error of $\sigma_z = 0.125\,z$ to simulate the redshift uncertainties, the model and the measurements agrees (Fig. 7). The Valiante et al. (2009) model poorly reproduces this observation. The Le Borgne et al. (2009) model agrees very well with the measurements, except at $z < 0.5$ and $z > 2.5$. The same observables was measured by Rodighiero et al. (2010). Their results agree with Le Floc'h et al. (2009), except at $z > 3$, where they are higher, perhaps because of a larger σ_z at high redshift.

We also compare the model with the redshift distribution of $S_{24} > 300 \mu$Jy sources measured by Le Floc'h et al. (2009), Rodighiero et al. (2010), and Desai et al. (2008). These different measurements disagree below $z = 0.5$. This difference could be due to the removal of the brightest optical sources (see previous paragraph). Our model overestimates the number of sources at $z < 0.5$ by a factor of 2. There is rather close agreements between the model and the measurements between $z = 0.5$ and $z = 2.5$, apart from a small overestimation by Valiante et al. (2009) near $z = 2$. At higher redshifts, the measurements are significantly higher than the models for possibly two reasons: an effect of the redshift uncertainties and the absence of AGNs in our model.

We compare with the Chapin et al. (2011) redshift distributions of the BLAST isolated sources at 250 μm, 350 μm, and 500 μm. This selection of isolated sources does not allow us to determine the effective size of the field. We thus normalized our model and the measured counts to have $\int \mathrm{d}N/\mathrm{d}z\mathrm{d}z = 1$. Our predicted redshift distribution globally fits the measurements, except at low z at 250 μm and 350 μm. This difference could be explained by the selection of isolated sources, which could miss sources in structures at low redshift. The other models (Le Borgne et al. 2009; Valiante et al. 2009) underpredict the number of sources at low z. Valiante et al. (2009) also slightly overpredicts the number of sources at $z \sim 1.5$.
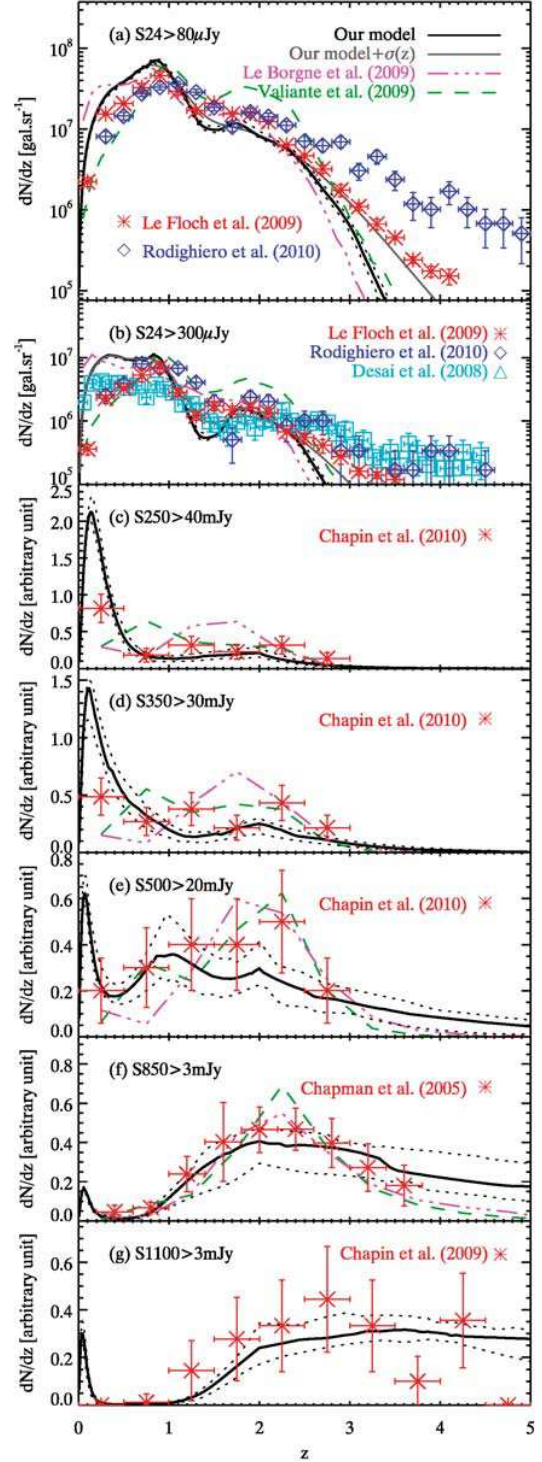
Fig. 7. Redshift distribution of the $S_{24} > 80 \mu$Jy **a)**, $S_{24} > 300 \mu$Jy **b)**, $S_{250} > 40$ mJy **c)**, $S_{350} > 30$ mJy **d)**, $S_{500} > 20$ mJy **e)**, $S_{850} > 3$ mJy **f)**, and $S_{1100} > 3$ mJy **g)** sources. These measurements are not fitted. Black solid line: our best-fit model. Black dotted line: 1-σ range of the model. Grey solid line: our best-fit model convolved by a Gaussian of $\sigma_z = 0.125z$. Purple three dot-dashed line: Le Borgne et al. (2009) model. Green dashed line: Valiante et al. (2009) model. Red asterisks: Le Floc'h et al. (2009) **a)**, **b)**, Chapin et al. (2011) **c)–e)**, Chapman et al. (2005) **f)** and Chapin et al. (2009) **g)** measurements. Blue diamonds: Rodighiero et al. (2010) measurements **a)**, **b)**. Cyan squares: Desai et al. (2008) measurements **b)**.

Table 3. Level of the non-correlated fluctuations of the CIB at different wavelengths and comparison with the predictions of the model.

Wavelength	Reference	S_{cut}	$P_{SN,mes}$	$P_{SN,model}$	$\langle z_{model} \rangle$
μm		mJy	Jy^2 sr^{-1}	Jy^2 sr^{-1}	
60	Miville-Deschênes et al. (2002)	1000	1600 ± 300	2089 ± 386	0.20 ± 0.01
90	Matsuura et al. (2011)	20	360 ± 20	848 ± 71	0.79 ± 0.03
100	Miville-Deschênes et al. (2002)	700	5800 ± 1000	7364 ± 1232	0.38 ± 0.03
160	Lagache et al. (2007)	200	9848 ± 120	10834 ± 3124	0.73 ± 0.06
250	Viero et al. (2009)	500	11400 ± 1000	11585 ± 2079	0.81 ± 0.08
350	Viero et al. (2009)	400	6300 ± 500	5048 ± 1083	1.17 ± 0.12
500	Viero et al. (2009)	–	2700 ± 200	1677 ± 484	1.59 ± 0.21
1363	Hall et al. (2010)	15	17 ± 2	10 ± 3	4.07 ± 0.24

Notes. The uncertainties on the model predictions take into account the uncertainties on γ_b. The mean redshift $\langle z_{model} \rangle$ of the contribution to the fluctuations is a prediction of the model.

We compared the redshift distribution of the SCUBA sources at 850 μm with the prediction of our model. We used the selection-corrected measurements of Chapman et al. (2005) adopted by Marsden et al. (2011). All the models agree with this measurement.

We also compared the predictions of our model with the redshift distribution of the sources detected at 1.1 mm by AzTEC (Chapin et al. 2009). A significant fraction of the sources detected at this wavelength (10 over 28) are not identified, and the selection is not performed in term of flux, but signal-to-noise ratio. Consequently, the normalization of the redshift distribution is unknown. We thus use the same normalization than for the BLAST redshift distributions ($\int dN/dz dz = 1$). The behavior predicted by our model agrees well with the observations.

Jauzac et al. (2011) measured the contribution of the $S_{24} > 80 \mu$Jy to the CIB at 70 and 160 μm as a function of the redshift. Their stacking analysis allows us to check the total far-infrared (FIR) emission of the faint sources not resolved at these wavelengths. Our model agrees well with their results, except near $z = 0.5$ (see Fig. 8), where their too low data points could come from a large-scale underdensity in the COSMOS field at this redshift. The Le Borgne et al. (2009) model overpredicts the contribution of the 24 μm sources at $z > 1$. The Valiante et al. (2009) model does not reproduce the trend of these measurements. Franceschini et al. (2010) underestimate the contribution of the local sources and overestimate the contribution of $z \sim 1$ sources.

5.6. Comparison with the measured Poisson fluctuations of the CIB

Table 3 summarizes the recent measurements of the non-correlated fluctuations of the CIB (P_{SN}) and the predictions of our model. We note that P_{SN} depends strongly on the $S_{\nu,cut}$, the flux density at which the resolved sources are cleaned. We agree with the measurements of Miville-Deschênes et al. (2002) at 60 μm and 100 μm, Lagache et al. (2007) at 160 μm, and Viero et al. (2009) at 250 μm and 350 μm. We found a value 35% lower than Viero et al. (2009) at 500 μm. This is consistent with the slight underestimation of the counts at 500 μm by our model. Our model is also about 40% lower than the SPT measurements at 1.36 mm (Hall et al. 2010), possibly because of a lack of faint sources at high redshift in our model. We also disagree with the results of Matsuura et al. (2011) at 90 μm within a factor of 2. Nevertheless, they cleaned all the detected sources without using a fixed cut in flux. We took their "mean" value of 20 mJy for the flux cut. The high sensitivity of the measurements to the flux cut could thus explains this difference (for instance, a decrease
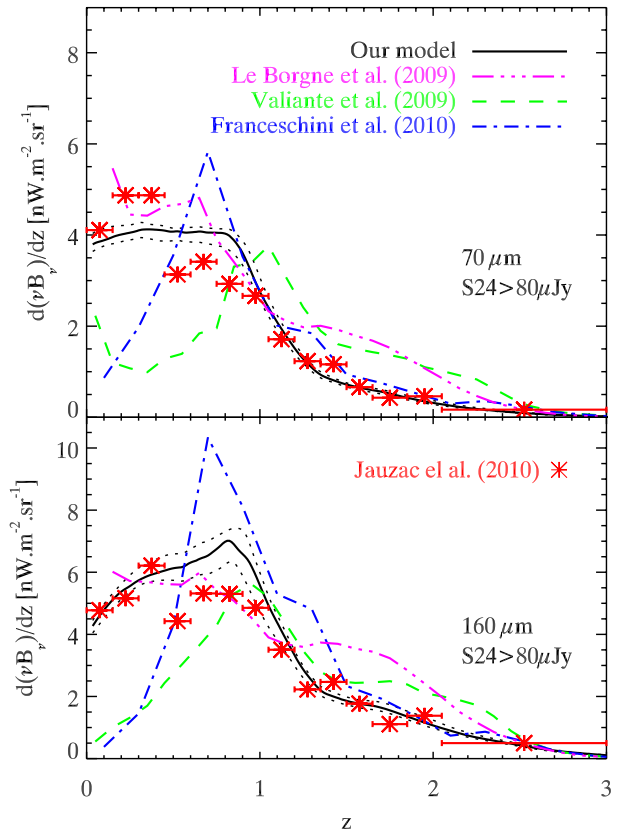
Fig. 8. Differential contribution of the $S_{24} > 80 \mu$Jy sources to the CIB as a function of the redshift at 70 μm (*upper panel*) and 160 μm (*lower panel*). Red asterisks: measurement by stacking in the COSMOS field (Jauzac et al. 2011). Black solid line: our model (1-σ limit in black dotted line). Purple three dot-dashed line: Le Borgne et al. (2009) model. Green dashed line: Valiante et al. (2009) model. Blue dot-dashed line: Franceschini et al. (2010) model.

in the flux cut by 25% leads to a decrease of the fluctuations of 19%).

We also computed the mean redshift at which the fluctuations are emitted with

$$\langle z \rangle = \frac{\int_0^\infty z \frac{dP_{SN}}{dz} dz}{\int_0^\infty \frac{dP_{SN}}{dz} dz}. \tag{17}$$

The results are written in Table 3. As expected, the mean redshift increases with the wavelength. Studying the long wavelengths is thus very useful for probing high redshift populations.

5.7. Comparison with the pixel histogram of the BLAST maps

The quality of our counts at low fluxes in the sub-mm range can be tested using a $P(D)$ analysis (Condon 1974; Patanchon et al. 2009; Glenn et al. 2010). Without instrumental noise, the probability density of the signal in a pixel of the map, $P(D)$, is given by

$$P(D) = \int_0^\infty \left[\exp\left(\int_0^\infty R(x)e^{i\omega x}dx - \int_0^\infty R(x)dx \right) \right] e^{-i\omega D}d\omega, \tag{18}$$

where $R(x)$ is defined by

$$R(x) = \int \frac{1}{b}\frac{dN}{dS_\nu}\left(\frac{x}{b}\right)d\Omega. \tag{19}$$

This probability distribution must be convolved with the distribution of the instrumental noise. We also subtract the mean of this distribution.

We tested our model by comparing with the deepest part of the observations of the CDFS by the BLAST team. We retained only the pixels in the map with a coverage larger than 90% of the maximum coverage. We smoothed the signal, noise, and beam map by a Gaussian kernel of the same full width at half maximum than the BLAST beam. This smoothing reduces the effect of the instrumental noise (Patanchon et al. 2009). Our model predictions and the BLAST pixel histograms at 250 μm, 350 μm, and 500 μm are shown in Fig. 9. The uncertainties in the model predictions take into account the BLAST calibration uncertainties (Truch et al. 2009). The model agrees rather well with the data. Nevertheless, the measured histogram is slightly broader than the predictions of the model, especially at 500 μm. It is consistent with the slight underestimation by our model of the counts at 500 μm (the higher the counts, the larger the histogram). The clustering of the galaxies (neglected in this analysis) tends to enlarge the histogram by about 10% and could also contribute to this disagreement (Takeuchi & Ishii 2004; Patanchon et al. 2009; Glenn et al. 2010). The Valiante et al. (2009) model reproduce the BLAST pixel histograms very well. Le Borgne et al. (2009) and Franceschini et al. (2010) over-predict the number of bright pixels at 250 μm and 350 μm ($S_\nu > 50$ mJy). It is consistent with these authors' overprediction of the counts at high flux (Oliver et al. 2010; Glenn et al. 2010).

5.8. Degeneracies between parameters

The Pearson correlation matrix of our model is given in Table 4. We found a very strong anti-correlations both between σ and $L_\star(z = 0)$ (–0.90) and between $L_\star(z = 0)$ and $\phi_\star(z = 0)$ (–0.85). These classical strong correlations are due to the choice of the LF parametrisation. There are also very strong degeneracies between the evolution in density and luminosity of the LF: –0.81 between 0 and the first break; –0.67 between the two breaks; and –0.76 after the second break.

There are some slight degeneracies between the calibration factors. The *Spitzer* calibration parameters are correlated (0.68 between 24 μm and 70 μm, 0.73 between 24 μm and 160 μm, and 0.62 between 70 μm and 160 μm). The other correlations implying a calibration factor are between –0.6 and 0.6.
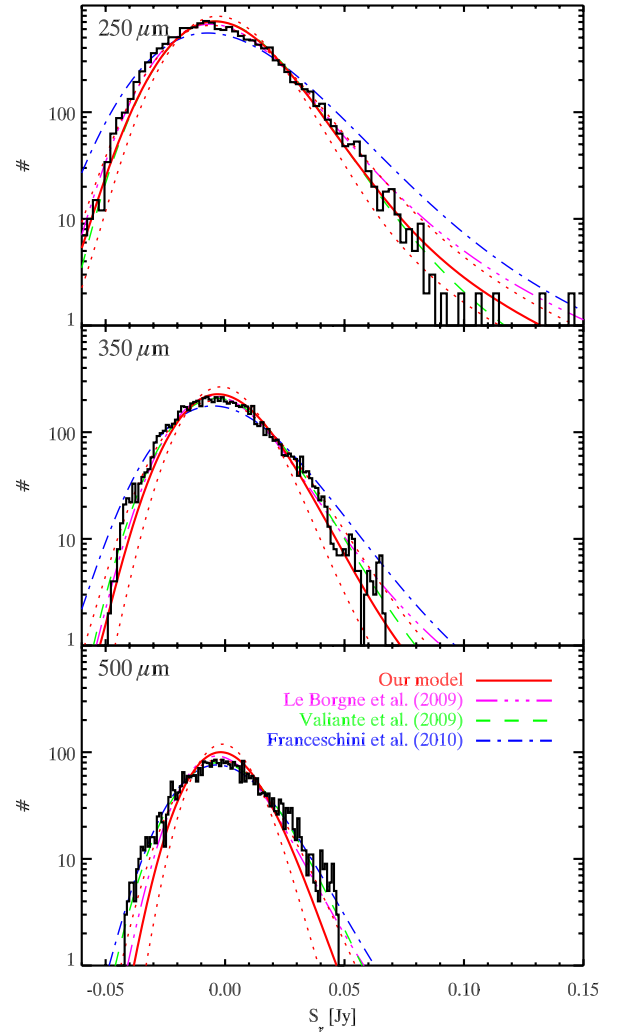

Fig. 9. Comparison with the BLAST pixel histogram at 250 μm (*upper panel*), 350 μm (*middle panel*) and 500 μm (*lower panel*). Black histogram: histogram of the values of the central part of the BLAST beam-smoothed map in Jy/beam. Red solid line: distribution predicted by our model using a $P(D)$ analysis. Our analysis does not include the clustering. Purple three dot-dashed line: Le Borgne et al. (2009) model. Green dashed line: Valiante et al. (2009) model. Blue dot-dashed line: Franceschini et al. (2010) model.

The marginalized probability distributions of each parameter and the 1, 2, and 3-σ confidence regions for each pair of parameters are plotted in Fig. 10. Some distributions are not Gaussian. It thus justifies the use of a MCMC algorithm.

6. Interpretation of the results

6.1. Evolution of the luminosity function

Our model uses a very strong evolution of the bolometric infrared luminosity function to reproduce the infrared observations. The characteristic luminosity ($L_\star$) has strongly decreased between $z = 2$ and now, by about a factor of 50 from $z = 2$ to 0. The characteristic density ($\phi_\star$) increases strongly between $z = 2$ and $z = 1$ and slightly decreases between $z = 1$ and now. At $z > 2$, the model is compatible with no evolution in luminosity
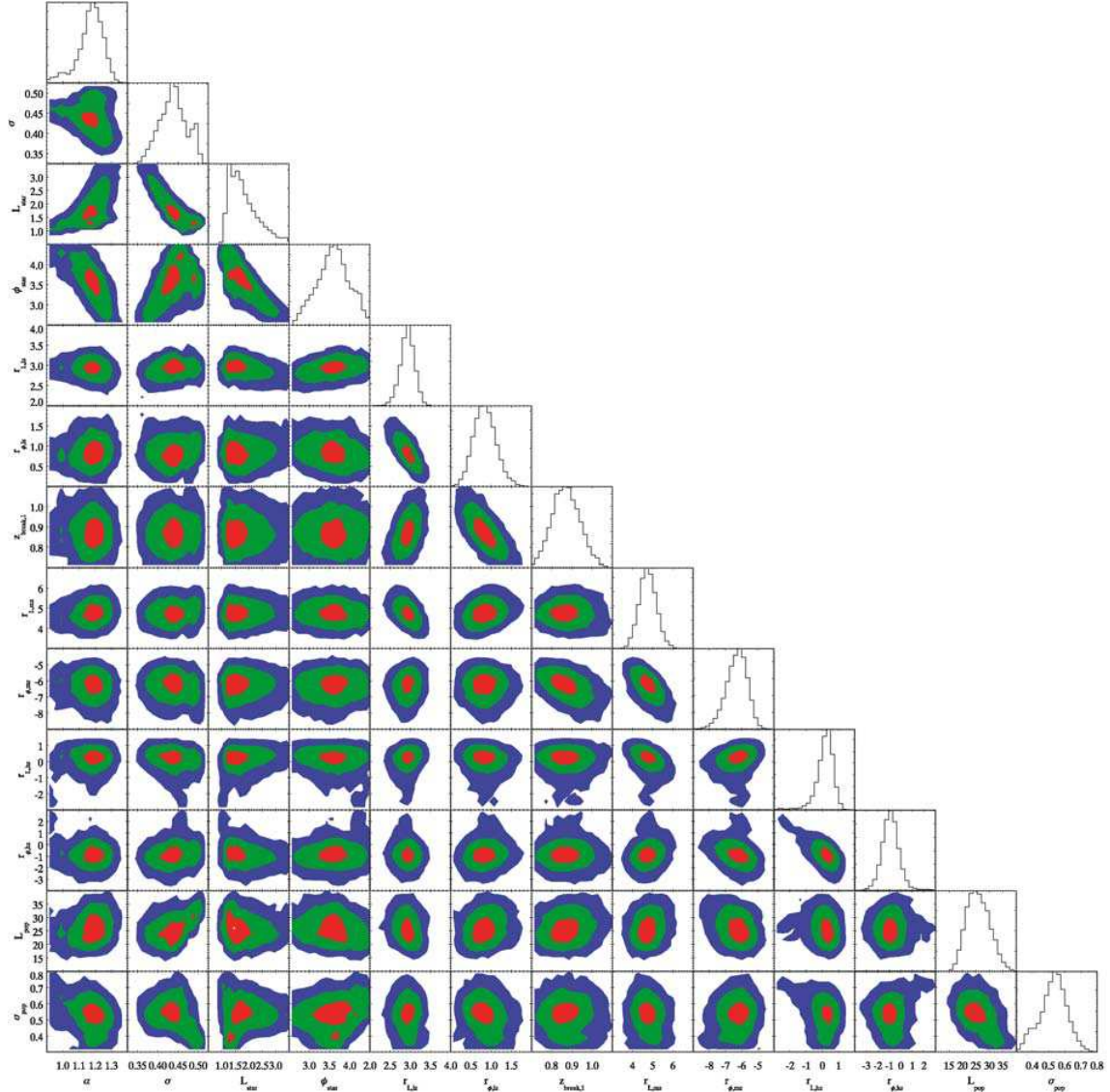
Fig. 10. Diagonal plots: marginalized probability distributions of each parameters deduced from the MCMC. Non-diagonal plots: 1-σ (red), 2-σ (green), and 3-σ (blue) regions for each pair of parameters). From left to right: α, σ, $L_\star$, $\phi_\star$, $r_{L_\star,lz}$, $r_{\mathrm{phi}_\star,lz}$, $z_{\mathrm{break},1}$, $r_{L_\star,mz}$, $r_{\mathrm{phi}_\star,mz}$, $r_{L_\star,hz}$, $r_{\mathrm{phi}_\star,hz}$, L_{pop}, and σ_{pop} (cf. Table 1).

and a slight decrease in the density as redshift increases. The evolution of these two parameters are plotted in Fig. 11.

We compared our results with the measurements of Caputi et al. (2007) performed from MIPS 24 μm observations and the measurement of Magnelli et al. (2009) obtained using MIPS 70 μm observations. These two works used a stacking analysis to measure the faintest points. The evolutions of $L_\star$ and $\phi_\star$ only marginally agree with these two works. Nevertheless, they use different fixed values of σ and α and an extrapolation from the monochromatic luminosity to L_{IR}. These choices could imply some biases. We found as Caputi et al. (2007) a strong negative evolution in density between $z \sim 1$ and $z \sim 2$, these authors finding an evolution in $(1 + z)^{-3.9 \pm 1.0}$ compared to our $(1 + z)^{-6.2 \pm 0.5}$. Nevertheless, our value is probably biased by our non-smooth parametrization. This evolution is discussed in details by Caputi et al. (2007).

Reddy et al. (2008) claimed that $\alpha \sim 1.6$ at $z > 2$. However, we do not need to invoke an evolution of α and σ to reproduce the observations. Nevertheless, the infrared measurements are not sufficiently deep to constrain accurately any evolution of α.

### 6.2. Evolution of the dust-obscured star formation rate

The bolometric infrared luminosity density (ρ_{IR}) can be deduced from the bolometric infrared LF. Our local value of ρ_{IR} ($(1.05 \pm 0.05) \times 10^8$ $L_\odot$ Mpc^{-3}) agrees with the Vaccari et al. (2010) measurements ($1.31^{+0.24}_{-0.21} \times 10^8$ $L_\odot$ Mpc^{-3}). We also agree well with higher redshift measurements of Rodighiero et al. (2010) and Pascale et al. (2009, see Fig. 12). The infrared luminosity density can be converted into star formation rate density (SFRD) using the conversion factor 1.7×10^{-10} $M_\odot$ yr^{-1} $L_\odot^{-1}$ (Kennicutt 1998). The SFRD derived from our model agrees rather well with the Hopkins & Beacom (2006) fit to the optical and infrared measurements.

We also determined the contribution of the different ranges of luminosity to the bolometric infrared luminosity density

**Table 4.** Pearson correlation matrix for our model.

	α	σ	$L_\star(z=0)$	$\phi_\star(z=0)$	$r_{L_\star,lz}$	$r_{\mathrm{phi}_\star,lz}$	$z_{\mathrm{break},1}$	$r_{L_\star,mz}$	$r_{\mathrm{phi}_\star,mz}$	$r_{L_\star,hz}$	$r_{\mathrm{phi}_\star,hz}$	L_{pop}	σ_{pop}
α	1.00	−0.48	0.71	−0.75	0.02	−0.06	0.04	0.14	−0.16	−0.04	0.11	−0.02	0.05
σ	−0.48	1.00	−0.90	0.62	−0.03	0.15	−0.06	0.10	0.05	−0.20	0.12	0.48	−0.37
$L_\star(z=0)$	0.71	−0.90	1.00	−0.85	−0.14	−0.03	0.07	0.00	−0.11	0.11	−0.04	−0.19	0.20
$\phi_\star(z=0)$	−0.75	0.62	−0.85	1.00	0.22	−0.15	−0.05	0.04	0.08	−0.04	−0.09	−0.11	−0.01
$r_{L_\star,lz}$	0.02	−0.03	−0.14	0.22	1.00	−0.81	0.51	−0.44	0.10	0.14	−0.12	−0.27	0.13
$r_{\mathrm{phi}_\star,lz}$	−0.06	0.15	−0.03	−0.15	−0.81	1.00	−0.78	0.18	0.07	−0.08	0.13	0.18	−0.17
$z_{\mathrm{break},1}$	0.04	−0.06	0.07	−0.05	0.51	−0.78	1.00	0.05	−0.51	−0.09	0.07	0.12	0.12
$r_{L_\star,mz}$	0.14	0.10	0.00	0.04	−0.44	0.18	0.05	1.00	−0.67	−0.43	0.29	0.05	−0.09
$r_{\mathrm{phi}_\star,mz}$	−0.16	0.05	−0.11	0.08	0.10	0.07	−0.51	−0.67	1.00	0.35	−0.41	−0.04	−0.07
$r_{L_\star,hz}$	−0.04	−0.20	0.11	−0.04	0.14	−0.08	−0.09	−0.43	0.35	1.00	−0.76	−0.20	−0.26
$r_{\mathrm{phi}_\star,hz}$	0.11	0.12	−0.04	−0.09	−0.12	0.13	0.07	0.29	−0.41	−0.76	1.00	0.11	0.18
L_{pop}	−0.02	0.48	−0.19	−0.11	−0.27	0.18	0.12	0.05	−0.04	−0.20	0.11	1.00	−0.39
σ_{pop}	0.05	−0.37	0.20	−0.01	0.13	−0.17	0.12	−0.09	−0.07	−0.26	0.18	−0.39	1.00

Notes. The part of the matrix concerning the calibration factors is not written to save space.
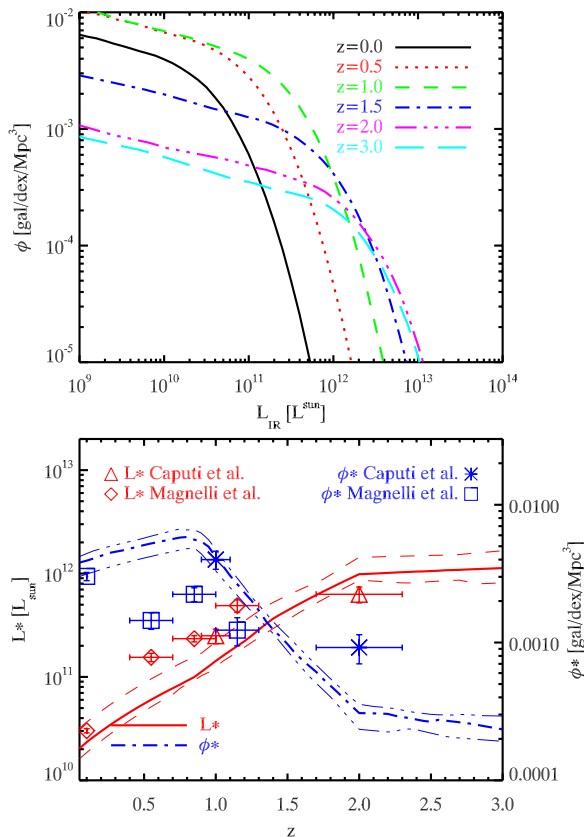
Fig. 11. Evolution of the bolometric infrared luminosity function with redshift. *Upper panel*: bolometric LF at $z = 0$ (solid line), $z = 0.5$ (dot line), $z = 1$ (dashed line), $z = 1.5$ (dot-dash line), $z = 2$ (3-dot-dash line), and $z = 3$ (long dashed line). Lower panel: Evolution of the $L_\star$ (red solid line) and $\phi_\star$ (blue dot-dash line) parameter as a function of redshift and 1-σ confidence region. The measurement of $L_\star$ by Caputi et al. (2007) (triangles) using 24 μm obervations and Magnelli et al. (2009) (diamonds) using 70 μm observations are plotted in red. The measurement of $\phi_\star$ by Caputi et al. (2007) (cross) and Magnelli et al. (2009) (square) are in blue.

(normal: $L_{\mathrm{IR}} < 10^{11}\,L_\odot$, LIRG: $10^{11} < L_{\mathrm{IR}} < 10^{12}\,L_\odot$, ULIRG: $10^{12} < L_{\mathrm{IR}} < 10^{13}\,L_\odot$, HyLIRG: $L_{\mathrm{IR}} > 10^{13}\,L_\odot$). Between $z = 0$ and 0.5, the infrared luminosity density is dominated by normal galaxies ($L_{\mathrm{IR}} < 10^{11}\,L_\odot$). Their contribution
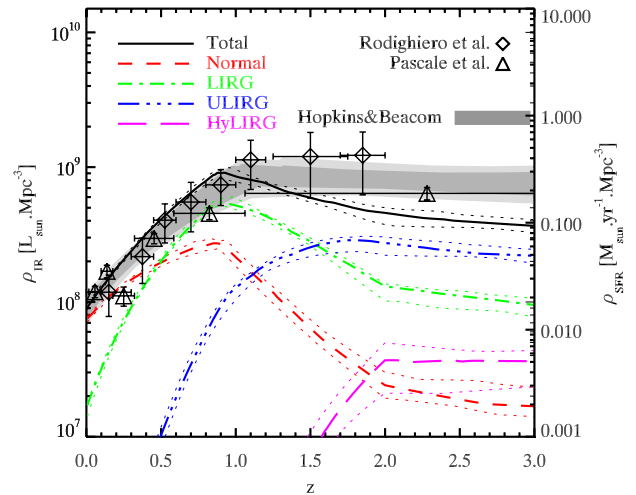
Fig. 12. Evolution of the bolometric infrared luminosity density (black solid line) as a function of the redshift. The contribution of normal galaxies ($L_{\mathrm{IR}} < 10^{11}\,L_\odot$), LIRG ($10^{11} < L_{\mathrm{IR}} < 10^{12}\,L_\odot$), ULIRG ($10^{12} < L_{\mathrm{IR}} < 10^{13}\,L_\odot$), and HyLIRG ($L_{\mathrm{IR}} > 10^{13}\,L_\odot$) are plotted with short-dashed, dot-dash, three-dot-dash, and long-dashed line respectively. The measurements of Rodighiero et al. (2010) using the MIPS 24 μm data are plotted with diamonds and Pascale et al. (2009) ones using a BLAST stacking analysis with triangles. The Hopkins & Beacom (2006) fit to the optical and infrared measurement is plotted with a dark grey area (1-σ) and a light grey area (3-σ).

decreases slowly with redshift because of the evolution of the LF seen in Fig. 11. Between $z = 0.5$ and 1.5, the infrared output is dominated by the LIRG. At higher redshift, it is dominated by ULIRGs. The HyLIRGs never dominate and account for some percent at high redshift. A physical cutoff at very high luminosity would this not strongly change the infrared density evolution.

Following our model, the number of very bright objects ($>10^{12.5}\,L_\odot$) is maximal around $z = 2$ (see Fig. 11). These objects could be very massive galaxies observed during their formation in the most massive dark matter halos. Among other analyses, the study of the spatial distribution of the galaxies will help us to confirm or exclude this scenario (Penin et al., in prep.).

Around $z = 1$, the number of very bright objects is lower than at higher redshift, but the number of LIRGs is about one order of magnitude larger. From $z = 1$ to now, the infrared output has decreased by about one order of magnitude. Our model describes

only this evolution and we need physical models to understand why, in contrast to today, the star formation at high redshift is dominated by a few very-quickly-star-forming galaxies, when the associated dark matter halos grew by hierarchical merging (Cole et al. 2000; Lanzoni et al. 2005). We also need to explain the decrease in the star formation since $z = 1$, the main candidates being the feedback of AGNs and starbursts (e.g. Baugh 2006) and/or the lack of gas.

6.3. CIB SED

The value of the CIB at different wavelengths predicted by the model is given in Table 5. We found a CIB integrated value (over the 8−1000 μm range) of 23.7 ± 0.9 nW m^{-2} sr^{-1}, which agrees with the 24−27.5 nW m^{-2} sr^{-1} range of Dole et al. (2006).

We compared the CIB spectrum found with our model with the measurements (see Fig. 13). Our model is always higher than the lower limit given by the stacking. The Marsden et al. (2009) limits are very stringent. Nevertheless, they could be overestimated because of the contamination due to clustering (Bavouzet 2008; Fernandez-Conde et al. 2010; Béthermin et al. 2010b). Our model is compatible with the upper limit given by the absorption of the TeV photons by photon-photon interaction with the CIB (see Sect. 7.2). We globally agree with the DIRBE/WHAM (Lagache et al. 2000) and AKARI (Matsuura et al. 2011) absolute measurement, except at 90 μm (AKARI) and 100 μm (DIRBE/WHAM) where the measurements are significantly higher than our model. These measurements need an accurate subtraction of both the zodiacal light and the galactic emissions and an accurate inter-calibration between DIRBE and FIRAS. A bad removal of the zodiacal light might explain this disagreement (Dole et al. 2006). At longer wavelengths, we closely agree with the FIRAS absolute measurements of Lagache et al. (2000).

We separated the contribution of the infrared galaxies to the CIB to four redshift slices, each slice corresponding to about a quarter of the age of the Universe (Fig. 13). Between 8 and 30 μm, we can see a widely varying behavior of each slice caused by the PAH emission bands. The total CIB is smoother. The $0 < z < 0.3$ slice dominates the spectrum only near 8 μm because of the strong PAH emission at this rest-frame wavelength. This slice, where the infrared luminosity density is at its lowest, has a minor contribution at the other wavelengths. The $0.3 < z < 1$ slice dominates the spectrum between 10 and 350 μm. The sub-mm and mm wavelengths are dominated by the sources lying at higher redshift ($z > 2$, see Lagache et al. 2005) because of the redshift effects that shift the peak of emission around rest-frame 80 μm in the sub-mm. The mean redshift of the contribution to the CIB is written in Table 5 and computed with

$$\langle z \rangle = \frac{\int_0^\infty z \frac{dB_\nu}{dz} dz}{\int_0^\infty \frac{dB_\nu}{dz} dz}.$$ (20)

We also separate the contribution of the different infrared luminosity classes. The normal galaxies and LIRGs dominate the background up to 250 μm, which is compatible these populations being dominant ones at low redshift. At longer wavelengths, the redshift effects tend to select high redshift sources, LIRGs and ULIRGs each being responsible for about half of the CIB. The HyLIRG have only a small contribution (<10%) including in the mm range (Fig. 13, bottom).
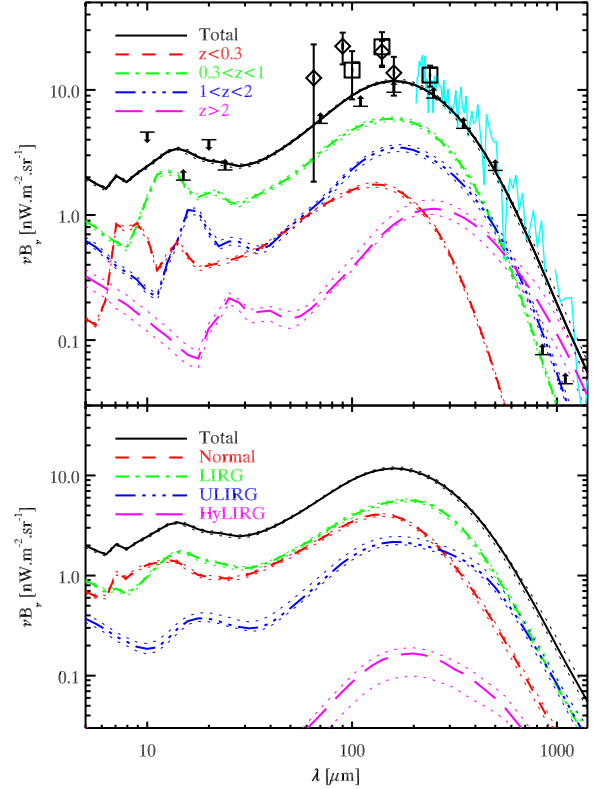
Fig. 13. *Upper panel*: contribution to the CIB per redshift slice. Black solid line: CIB spectrum predicted by the model. Red short-dashed line: contribution of the galaxies between $z = 0$ and 0.3. Green dot-dash line: same thing between $z = 0.3$ and 1. Blue three dot-dash line: same thing between $z = 1$ and 2. Purple long-dashed line: contribution of the galaxies at redshift higher than 2. Black arrows: lower limits coming from the number counts at 15 μm (Hopwood et al. 2010) and 24 μm (Béthermin et al. 2010a) and the stacking analysis at 70 μm (Béthermin et al. 2010a), 100 μm, 160 μm (Berta et al. 2010), 250 μm, 350 μm, 500 μm (Marsden et al. 2009), 850 μm (Greve et al. 2010), and 1.1 mm (Scott et al. 2010) and upper limits coming from absorption of the TeV photons of Stecker & de Jager (1997) at 20 μm and Renault et al. (2001) between 5 μm and 15 μm. Black diamonds: Matsuura et al. (2011) absolute measurements with AKARI. Black square: Lagache et al. (2000) absolute measurements with DIRBE/WHAM. Cyan line: Lagache et al. (2000) FIRAS measurement. *Lower panel*: contribution to the CIB of the normal galaxies (red short-dashed line), LIRGs (green dot-dash line), ULIRGs (blue three dot-dash line), HyLIRG (purple long-dashed line), and all the galaxies (black solid line).

7. Predictions
7.1. Confusion limit

The confusion limit can be defined in several ways. The radioastronomers classically use a source density criteria, where the confusion limit is the flux cut for which a critical density of sources is reached. The choice of this critical density is not trivial. We follow the approach of Dole et al. (2003). The source density limit N_{SDC} is reached when there is a probability P of having another source in a k θ_{FWHM} radius (where θ_{FWHM} is the full width at half maximum of the beam profile). Dole et al. (2003) show that

$$N_{SDC} = -\frac{\log(1 - P)}{\pi k^2 \theta_{FWHM}^2}.$$ (21)

We chose $P = 0.1$ and $k = 0.8$ following Dole et al. (2003).

Table 5. Surface brightness of the CIB and mean redshift $\langle z \rangle$ of the contribution to the CIB at different wavelengths as predicted by the model.

Wavelength	CIB	CIB	$\langle z \rangle$
μm	nW m^{-2} sr^{-1}	MJy sr^{-1}	
15	$3.294^{+0.105}_{-0.128}$	$0.016^{+0.001}_{-0.001}$	$0.820^{+0.026}_{-0.018}$
24	$2.596^{+0.076}_{-0.139}$	$0.021^{+0.001}_{-0.001}$	$0.894^{+0.025}_{-0.029}$
70	$5.777^{+0.165}_{-0.067}$	$0.135^{+0.004}_{-0.002}$	$0.773^{+0.022}_{-0.021}$
100	$9.014^{+0.231}_{-0.125}$	$0.300^{+0.008}_{-0.004}$	$0.829^{+0.023}_{-0.024}$
160	$11.771^{+0.382}_{-0.318}$	$0.628^{+0.020}_{-0.017}$	$0.947^{+0.032}_{-0.019}$
250	$9.100^{+0.395}_{-0.382}$	$0.758^{+0.033}_{-0.032}$	$1.124^{+0.053}_{-0.021}$
350	$5.406^{+0.190}_{-0.417}$	$0.631^{+0.022}_{-0.049}$	$1.335^{+0.075}_{-0.060}$
500	$2.237^{+0.077}_{-0.217}$	$0.373^{+0.013}_{-0.036}$	$1.680^{+0.124}_{-0.122}$
850	$0.374^{+0.057}_{-0.042}$	$0.106^{+0.016}_{-0.012}$	$2.444^{+0.292}_{-0.192}$
1100	$0.139^{+0.031}_{-0.017}$	$0.051^{+0.011}_{-0.006}$	$2.833^{+0.341}_{-0.201}$

This source density criterion does not take into account the contributions of the sources fainter than the flux limit. We also estimated the photometric confusion noise based on the $P(D)$ analysis (see Sect. 5.7). The $P(D)$ distribution in the absence of instrumental noise is non-Gaussian and have a large tail at bright flux. Thus, the standard deviation is not a good estimator of the confusion noise. We chose to compute the interquartile interval of the $P(D)$ divided by 1.349. With this definition, the value of the confusion noise is exactly σ in the Gaussian case, and we are less sensitive to the bright outliers.

These two estimators can be computed from the counts predicted by our model. We assume that the sources are point-like. The confusion noise found for large telescopes at short wavelengths ($< 8\ \mu$m for a 0.85 m-diameter telescope like *Spitzer* and $< 35\ \mu$m for a 3.29 m-diameter telescope like *Herschel*) are thus underestimated. For this reason, we do not estimate the confusion levels for beams smaller than 2 arcsec.

Figure 14 (upper panel) represents the confusion noise, which agrees with the confusion noise measured by Frayer et al. (2009) and Nguyen et al. (2010) with *Spitzer*/MIPS and *Herschel*/SPIRE. Weiß et al. (2009) estimate that the confusion noise for a APEX/LABOCA map smoothed by the beam is 0.9 mJy/beam. We find 0.6 mJy/beam with the $P(D)$ approach.

We also compute the resolved fraction of the CIB by sources brighter than the confusion limit of Dole et al. (2003) (source density criterion) and the 5-$\sigma_{\rm conf}$ given by the $P(D)$. Figure 14 (lower panel) and Tables 6–10 summarize the results. The transition in the confusion regime between the source density limitation (short wavelengths) and the fluctuation limitation (long wavelengths) happens at 100 μm for *Spitzer*, 220 μm for *Herschel*, and 1120 μm for the JCMT (asterisks in the lower panel of Fig. 14). For larger antennas below 1.2 mm, the confusion is mainly due to the source density.

According to these results, at the confusion limit, *Herschel* can resolve 92%, 84%, 60%, 25.9%, 9.2%, and 3.3% of the CIB at 70 μm, 100 μm, 160 μm, 250 μm, 350 μm, and 500 μm, respectively. Nevertheless, owing to the blackbody emission of the telescope (about 60 K), very long integration times are needed to reach the confusion limit at short wavelengths. The confusion limit in PACS will only be reached in the ultra-deep region of the H-GOODS survey. The confusion limit will probably never be reached at 70 μm. A telescope of the same size as *Herschel* and a cold (5K) mirror, such as SPICA, could resolve almost all the CIB from the mid-infrared to 100 μm. A 25 m single-dish submm telescope such as the Cornell Caltech Atacama telescope

Table 6. Confusion noise and resolved fraction of the CIB at different wavelengths for a 0.85 m telescope (*Spitzer* like).

λ	$5\sigma_{\rm conf, P(D)}$	CIB fraction[a]	$S_{\rm conf, density}$	CIB fraction[b]
μm	mJy	%	mJy	%
24	5.62×10^{-2}	83.1	7.51×10^{-2}	72.3
70	3.09×10^{0}	51.5	2.88×10^{0}	48.8
100	1.38×10^{1}	36.3	1.15×10^{1}	36.1
160	5.84×10^{1}	12.3	3.43×10^{1}	17.2
250	1.06×10^{2}	3.2	4.41×10^{1}	6.9
350	1.13×10^{2}	0.8	3.57×10^{1}	3.0
500	9.18×10^{1}	0.2	2.24×10^{1}	1.4
850	4.12×10^{1}	100.0	9.25×10^{0}	0.7
1100	2.76×10^{1}	100.0	6.25×10^{0}	0.5

Notes. [a] Fraction of the CIB resolved at 5-$\sigma_{\rm conf}$. [b] Fraction of the CIB resolved at the flux limit.

Table 7. Confusion noise and resolved fraction of the CIB at different wavelengths for a 3.29 m telescope (*Herschel* like).

λ	$5\sigma_{\rm conf, P(D)}$	CIB fraction[a]	$S_{\rm conf, density}$	CIB fraction[b]
μm	mJy	%	mJy	%
70	7.95×10^{-2}	96.4	1.20×10^{-1}	91.8
100	5.13×10^{-1}	90.8	7.75×10^{-1}	83.9
160	5.01×10^{0}	67.8	5.93×10^{0}	59.8
250	1.75×10^{1}	25.9	1.28×10^{1}	29.6
350	2.30×10^{1}	9.2	1.28×10^{1}	15.8
500	2.08×10^{1}	3.3	9.24×10^{0}	8.7
850	1.13×10^{1}	1.5	3.88×10^{0}	4.4
1100	8.40×10^{0}	1.2	2.66×10^{0}	3.5

Notes. [a] Fraction of the CIB resolved at 5-$\sigma_{\rm conf}$. [b] Fraction of the CIB resolved at the flux limit.

Table 8. Confusion noise and resolved fraction of the CIB at different wavelengths for a 12.00 m telescope (APEX like).

λ	$5\sigma_{\rm conf, P(D)}$	CIB fraction[a]	$S_{\rm conf, density}$	CIB fraction[b]
μm	mJy	%	mJy	%
160	5.86×10^{-2}	99.4	5.55×10^{-2}	98.2
250	7.06×10^{-1}	94.2	1.11×10^{0}	85.6
350	2.08×10^{0}	77.9	2.57×10^{0}	63.2
500	3.05×10^{0}	50.0	2.57×10^{0}	41.8
850	2.19×10^{0}	23.6	1.24×10^{0}	22.9
1100	1.74×10^{0}	18.4	8.74×10^{-1}	18.6

Notes. [a] Fraction of the CIB resolved at 5-$\sigma_{\rm conf}$. [b] Fraction of the CIB resolved at the flux limit.

Table 9. Confusion noise and resolved fraction of the CIB at different wavelengths for a 15.00 m telescope (JCMT like).

λ	$5\sigma_{\rm conf, P(D)}$	CIB fraction[a]	$S_{\rm conf, density}$	CIB fraction[b]
μm	mJy	%	mJy	%
160	2.34×10^{-2}	99.8	1.04×10^{-2}	99.3
250	3.01×10^{-1}	97.6	4.48×10^{-1}	92.5
350	1.08×10^{0}	88.6	1.55×10^{0}	74.7
500	1.87×10^{0}	66.6	1.86×10^{0}	52.4
850	1.55×10^{0}	33.8	9.70×10^{-1}	29.4
1100	1.26×10^{0}	26.7	6.89×10^{-1}	24.1

Notes. [a] Fraction of the CIB resolved at 5-$\sigma_{\rm conf}$. [b] Fraction of the CIB resolved at the flux limit.
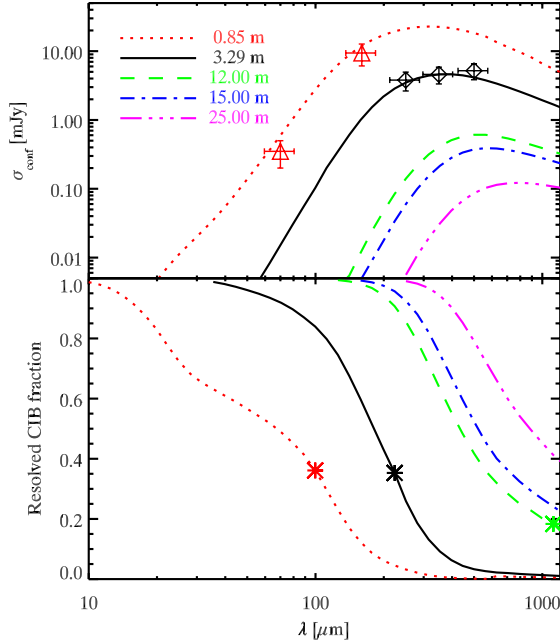
Fig. 14. *Upper panel*: 1-σ confusion noise as a function of the wavelength for different telescope diameters. We use the confusion noise given by the $P(D)$ method (see Sect. 7.1) for this plot. Red triangles: Frayer et al. (2009) *Spitzer*/MIPS confusion measurements. Black diamonds: Nguyen et al. (2010): *Herschel*/SPIRE confusion noise measurements (5-σ_{conf} cut). *Lower panel*: resolved fraction of the CIB by sources brighter than 5-σ confusion noise (fluctuations) and the source density limit. *Both panel*: Red dotted line: telescope with a diameter of 0.85 m such as Spitzer. Black solid line: 3.29 m telescope such as *Herschel*. Green dashed line: 12 m telescope such a Atacama pathfinder experiment (APEX). Blue dot-dashed line: 15 m telescope such as the JCMT. Purple three dot-dashed line: 25 m such as the CCAT project. Asterisks: transition between the source density limitation (short wavelengths) and the fluctuation limitation (long wavelengths).

Table 10. Confusion noise and resolved fraction of the CIB at different wavelengths for a 25.00 m telescope (CCAT-like).

λ	$5\sigma_{conf,P(D)}$	CIB fraction[a]	$S_{conf,density}$	CIB fraction[b]
μm	mJy	%	mJy	%
250	2.81×10^{-2}	99.8	1.32×10^{-2}	99.1
350	1.57×10^{-1}	98.5	2.12×10^{-1}	94.2
500	4.31×10^{-1}	92.6	6.09×10^{-1}	79.1
850	5.99×10^{-1}	64.6	4.62×10^{-1}	49.7
1100	5.39×10^{-1}	53.1	3.46×10^{-1}	41.2

Notes. [a] Fraction of the CIB resolved at 5-σ_{conf}. [b] Fraction of the CIB resolved at the flux limit.

(CCAT) project would be able to resolve more than 80% of the CIB up to 500 μm.

7.2. High energy opacity

The CIB photons can interact with TeV photons. The cross-section between a E_γ rest-frame high-energy photon and an infrared photon with a observer-frame wavelength λ_{IR}

interacting at a redshift z with an angle θ (and $\mu = \cos(\theta)$) is (Heitler 1954; Jauch & Rohrlich 1976)

$$\sigma_{\gamma\gamma}(E_\gamma, \lambda_{IR}, \mu, z) = H\left(1 - \frac{\epsilon_{th}}{\epsilon}\right) \frac{3\sigma_T}{16}(1 - \beta^2) \quad (22)$$

$$\times \left[2\beta(\beta^2 - 2) + (3 - \beta^4)\ln\left(\frac{1+\beta}{1-\beta}\right)\right] \quad (23)$$

with

$$\beta = \sqrt{1 - \frac{\epsilon_{th}}{\epsilon}}, \quad (24)$$

$$\epsilon_{th}(E_\gamma, \mu, z) = \frac{2(m_e c^2)^2}{E_\gamma(1-\mu)(1+z)}, \quad (25)$$

$$\epsilon(\lambda_{IR}, z) = \frac{hc(1+z)}{\lambda_{IR}}, \quad (26)$$

where σ_T is the Thompson cross-section (6.65×10^{-29} m^2), m_e the mass of the electrons, and H the Heaviside step function ($H(x) = 1$ if $x > 0$ and 0 else).

The optical depth $\tau(E_\gamma, z_s)$ for a photon observed at energy E_γ and emitted at a redshift z_s can be easily computed (Dwek & Krennrich 2005; Younger & Hopkins 2011; Domínguez et al. 2011) with

$$\tau(E_\gamma, z_s) = \int_0^{z_s} dz \frac{D_H}{\sqrt{\Omega_\Lambda + (1+z)^3 \Omega_m}}$$
$$\times \int_{-1}^1 d\mu \frac{1-\mu}{2} \int_{5\mu m}^\infty d\lambda_{IR} n_{\lambda_{IR}}(\lambda_{IR}, z)(1+z)^2 \sigma_{\gamma\gamma}(E_\gamma, \lambda_{IR}, \mu, z), \quad (27)$$

where $n_{\lambda_{IR}}(\lambda_{IR}, z)$ is the comoving number density of photons emitted at a redshift greater than z between λ_{IR} and $\lambda_{IR} + d\lambda_{IR}$. The 5 μm cut corresponds to the limit of the validity of our model. The number density of photons is computed with

$$n_{\lambda_{IR}}(\lambda_{IR}, z) = \frac{4\pi}{hc\lambda_{IR}}(B_{\nu,CIB} + B_{\nu,CMB}), \quad (28)$$

where $B_{\nu,CIB}$ is the CIB given by our model and $B_{\nu,CMB}$ is the brightness of a blackbody at 2.725 K corresponding to the cosmic microwave background (Fixsen 2009). Our predicted opacities do not take into account the absorption by the cosmic optical background photons (COB, $\lambda < 5$ μm). Younger & Hopkins (2011) showed that the contribution of the COB to the opacity is negligible for energies higher than 5 TeV.

We can determine up to which redshift the opacity stays lower than 1. We can thus define an horizon as a function of the energy, called the Fazio-Stecker relation. We can see in Fig. 15 that the observed energy cutoff of low-redshift blazars (Mkn 501, Aharonian et al. 1999; Mkn 421, Aharonian et al. 2002; and BL Lac 1ES 1959+650, Aharonian et al. 2003) is compatible with this relation.

7.3. Effect of the strong lensing on the number counts

The strongly-lensed fraction is the ratio of the counts of lensed sources to the total observed counts. Because the slope of the counts varies a lot with the flux and wavelength, this fraction depends on the flux and the wavelength (see Fig. 16). The strongly lensed fraction is always smaller than 2% below 250 μm and is thus negligible. At longer wavelengths, we predict a maximum of the strongly lensed fraction near 100 mJy. At 500 μm, about 15% of the sources brighter than 100 mJy are lensed. This fraction increases to 40% near 1 mm.
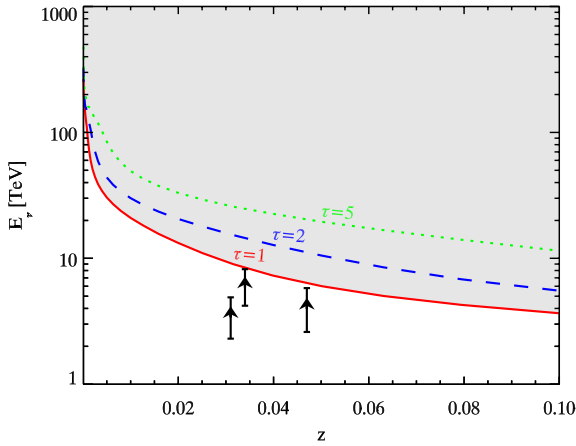
Fig. 15. Fazio-Stecker relation: energy at which the opacity reach a given τ as a function of redshift. This plot is done for $\tau = 1$ (red solid line), 2 (blue dashed line) and 5 (green dotted line). The data points are the cutoff energy of Mkn 501 (Aharonian et al. 1999), Mkn 421 (Aharonian et al. 2002) and Lac 1ES 1959+650 (Aharonian et al. 2003).
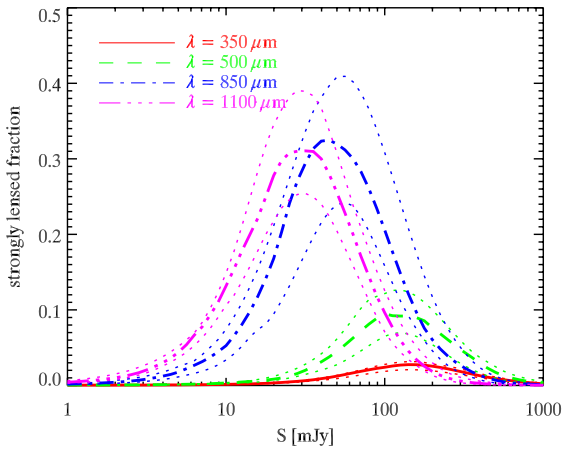
Fig. 16. Fraction of strongly lensed sources (magnification larger than 2) as a function of the flux at 350 μm (red solid line), at 500 μm (green dashed line), at 850 μm (blue dot-dashed line) and at 1.1 mm (purple three-dot-dashed line). The dotted lines represent the 1-σ confidence area of our model.

Our results can be compared with those of the Negrello et al. (2007) model. The two models predict that the lensed fraction as a function of the flux is a bump around 100 mJy. However, the amplitude of this bump predicted by the two models is significantly different. For instance, the maximum of the lensed fraction at 500 μm is 15% for our model and 50% for the Negrello et al. (2007) model. The slope between 10 and 100 mJy is steeper in Negrello et al. (2007) model than in ours and is incompatible with the measurements (Clements et al. 2010; Oliver et al. 2010; Glenn et al. 2010). The steeper the slope, the larger the lensed fraction. This explains why the Negrello et al. (2007) model predicts larger lensed fraction than ours. The probability of a source being lensed increases with its redshift. The differences in the redshift distributions of the models could also explain some of the differences in the lensed fraction.
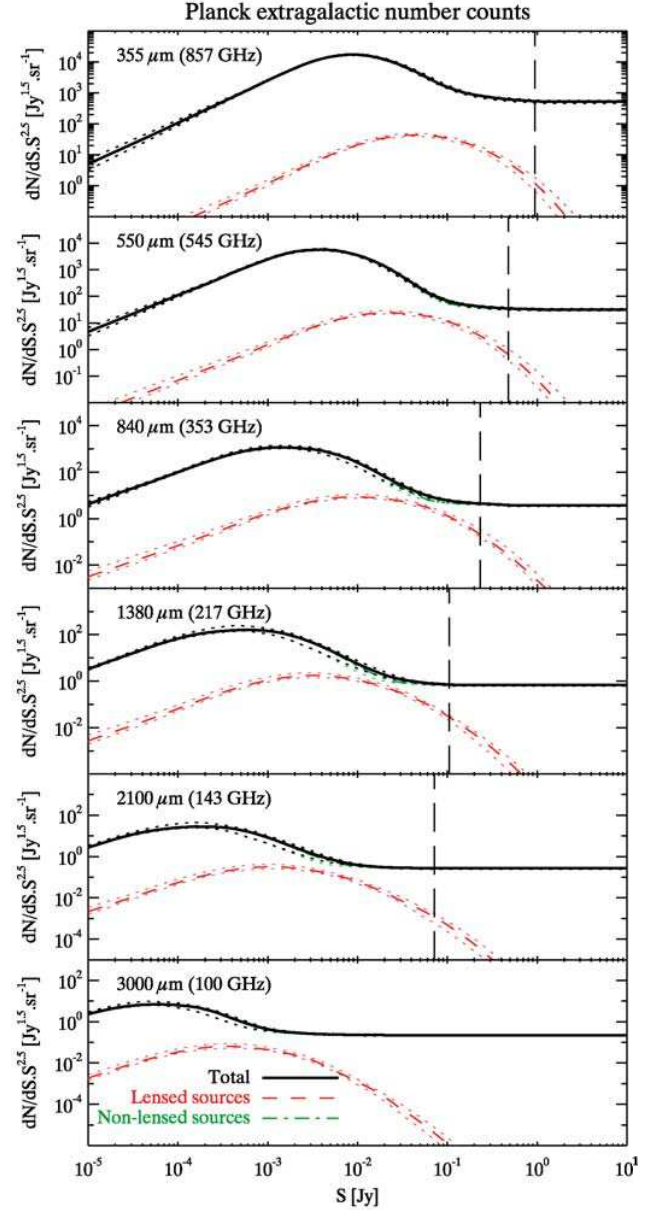
Fig. 17. Differential number counts in the *Planck* bands. These counts only take into account the individual star-forming galaxies. Black solid line: total contribution. Green dot-dashed line: contribution of the non-lensed sources. Red dashed line: contribution of the strongly-lensed sources. Dotted lines 1-σ contours. Vertical long-dahsed line: 5-σ limits (confusion+instrumental) of Fernandez-Conde et al. (2008) for a bias of 1.5.

Figure 6 shows the respective contribution of the lensed and non-lensed sources to the SPT counts of dusty sources without IRAS 60 μm counterparts at 1.38 mm (Vieira et al. 2010). According to the model, these counts are dominated by strongly-lensed sources above 15 mJy. These bright sources are thus very likely to correspond to strongly-lensed sub-mm galaxies.

We predicted on the contribution of the strongly-lensed sources to the *Planck* number counts (see Fig. 17) using Fernandez-Conde et al. (2008) 5-σ limits, because they take into account the effect of the clustering on the confusion noise. This

effect is non-negligible because of the large beam of *Planck*. We found that the contribution of the lensed sources to the *Planck* counts is negligible in all the bands (a maximum of 0.47 galaxies sr^{-1} at 550 μm). At high redshift, *Planck* will probably detect more small structures such as proto-clusters, than individual galaxies. *Planck* is thus not the best survey to find lensing candidates. Sub-mm surveys with a sensitivity near 100 mJy are more efficient. For instance, the *Herschel*-ATLAS survey should find 153 ± 26 and 411 ± 24 lensed sources with $S_{500} > 50$ mJy and $S_{350} > 50$ mJy, respectively, across 600 deg^2.

8. Discussion

8.1. Comparison with other backward evolution models

The evolution of the infrared luminosity density predicted by our model can be compared with the predictions of other backward evolution models. We find, like Franceschini et al. (2010), a strong increase in ρ_{IR} from $z = 0$ to $z = 1$, a break around $z = 1$, and a decrease at higher redshift. In contrast, the Valiante et al. (2009) and Le Borgne et al. (2009) models predict a maximum of infrared luminosity density around $z = 2$.

In a similar way to Le Borgne et al. (2009) and Franceschini et al. (2010), we found that LIRGs dominate infrared luminosity density around $z = 1$ and that ULIRGs dominate at redshift higher than 1.5. We also found as Le Borgne et al. (2009) that normal galaxies dominates ρ_{IR} only up to $z \sim 0.5$.

Our model and the Valiante et al. (2009) one use a similar parametrization of the LF evolution. Both models found a very strong evolution in luminosity up to $z = 2$ ($(1 + z)^{3.4}$ for the Valiante et al. (2009) model, which can be compared with $(1 + z)^{2.9 \pm 0.1}$ from $z = 0$ to 0.87 ± 0.05 and $(1 + z)^{4.7 \pm 0.3}$ from $z = 0.87 \pm 0.05$ to 2 for our model). At higher redshift, our model is compatible with no evolution and the Valiante et al. (2009) model predicts a slight decrease in $(1 + z)^{-1}$. Concerning the evolution in density, both models predicts an increase from $z = 0$ to $z \approx 1$ (proportional to $(1 + z)^2$ for the Valiante et al. (2009) model and $(1 + z)^{0.8 \pm 0.2}$ for our model) and a decrease at higher redshift ($(1 + z)^{-1.5}$ for the Valiante et al. (2009) model, $(1+z)^{-6.2 \pm 0.5}$ between $z = 0.87 \pm 0.5$ and $z = 2$ and $(1+z)^{-0.9 \pm 0.7}$ at $z > 2$ for our model). These two models thus agree on the global shape of the evolution of the LF, but disagree on the values of the coefficient driving it. There is in particular a large difference on the evolution density between $z \sim 1$ and $z \sim 2$. This difference could be explained by the different positions of the breaks. Nevertheless, the uncertainties on the Valiante et al. (2009) model are not estimated. It is thus difficult for us to draw any conclusion.

Valiante et al. (2009) and Franceschini et al. (2010) used AGNs to reproduce the infrared observations. Valiante et al. (2009) also used a temperature dispersion of the galaxies. Our model reproduce the same observations using neither AGNs nor temperature dispersion. This demonstrates that the AGN contribution and the temperature scatter cannot be accurately constrained by with this type of modeling.

8.2. Discriminating the models: smoking gun observations?

Although they use different galaxy populations and evolutions, the backward evolution models reproduce the number counts from the mid-IR to the mm domain in a reasonably good way. It is thus important to find new observables to discriminate between models.
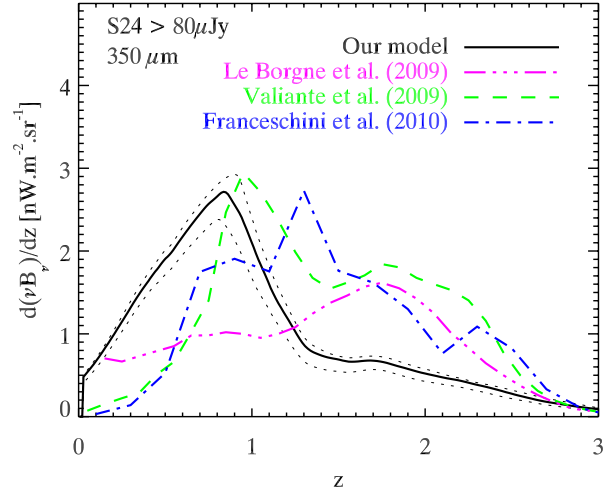
Fig. 18. Differential contribution of the $S_{24} > 80$ μJy sources to the CIB as a function of the redshift at 350 μm. Black solid line: Our model (1-σ limit in black dotted line). Purple three dot-dashed line: Le Borgne et al. (2009) model. Green dashed line: Valiante et al. (2009) model. Blue dot-dashed line: Franceschini et al. (2010) model.

The sub-mm redshift distributions of the bright sources are quite straightforward, but very discriminant observations. For instance, Fig. 7 shows a significant difference in the sub-mm redshift distributions predicted by the different models. The Chapin et al. (2011) measurements performed on one small field with a cut at high flux do not enable us to draw strong conclusions. *Herschel* will help us to increase the accuracy of the measured redshift distributions and estimate the cosmic variance in them. These constraints will be crucial for the next generation of models.

Jauzac et al. (2011) showed that the redshift distribution of the contribution of the 24 microns sources to CIB at 70 and 160 μm (d(νB_ν)/dz) also provides a strong constraint. Figure 18 shows the d(νB_ν)/dz at 350 μm. The different models make totally incompatible predictions in the sub-mm. An accurate measurement of d(νB_ν)/dz will thus be crucial for future models.

8.3. Limits of our model

Our model is a useful tool to make a first interpretation of the observations from the mid-infrared to the mm domain. Nevertheless, it is biased by some structural choice in its construction.

The choice of the parameters biases the results. For example, we have chosen the minimal number of parameters to reproduce the counts. If we had used more breaks in the evolution in both density and luminosity, the evolutions with redshift would have been smoother and the errors in the predictions would have been different. Our errors are just the statistical errors due to the determination of the parameter of a given model using the data. It does not include the uncertainty in our hypothesis about the evolution (such as α fixed) and the biases due to our choice of parameters (evolution in $(1 + z)^r$ with breaks). For instance, the strong decrease in density between $z \sim 0.9$ and $z = 2$ is probably an artifact caused by our choice of parametrization. In addition, our model of lensing is very simple and should be improved in the future. Nevertheless, the contribution of the lensing in the fitted data is low and the bias is thus negligible.

The backward evolution models gives a very limited interpretation of the data. They provide only a description of the evolution of the statistical properties of the infrared galaxies. The physical processes explaining the strong evolution of these objects are ignored. A more complex physical approach is thus necessary to deeply understand the history of the infrared galaxies. Nevertheless, our model is very useful for providing a rapid interpretation of new observations and predictions for future missions.

8.4. Perspectives

Our models fit the current data when we employ rather simple hypotheses. Nevertheless, the increasing accuracy of infrared observations will probably help us to improve the model. Additional model updates will be possible in the future.

The α and σ parameters are fixed, but it may be necessary to incorporate an evolution of the shape of the LF with the redshift. A Fisher matrix analysis shows that the evolution of α at high redshift cannot be constrained without deeper observations in the sub-mm. An evolution of σ could be constrained, but is not necessary to reproduce the current data.

The evolution of the parameters is very simple in the current version and could be updated by using more breaks or a smoother functional form.

The observations of *Herschel* will help us to improve the SED used in our model, and maybe enable us to determine the SED evolution with redshift. The temperature of the big grains and its dispersion will be measured more accurately. Nevertheless, this dispersion must be modeled with a limited number of templates to allow us to use an MCMC approach. This will be one of the future challenges of including it in our model.

Nevertheless, each refinement increases the number of free parameters of the model. It is important to limit the number of new parameters in comparison with the number of measurements.

9. Summary

– Our new parametric backward evolution model has enabled us to reproduce the number counts from 15 μm to 1.1 mm, the monochromatic LF, and the redshift distributions.
– We have found that our model predicts a strong evolution in the LF characteristic luminosity up to $z = 2$ and a strong decrease in density from $z = 1$ to $z = 2$. We predict that the number of HyLIRG reaches a maximum around $z = 2$.
– We have found that normal galaxies, LIRGs, and ULIRGs dominates the infrared output at $z = 0$, $z = 1$, and $z = 2$, respectively. The HyLIRG accounts for a small fraction ($<10\%$) at all redshifts.
– We have reproduced the CIB spectrum and predicted the contributions per redshift and luminosity slice. We found that the mid- and far-infrared part of the CIB are mainly emitted by the normal galaxies and LIRG. The sub-mm part is mainly due to LIRGs and ULIRGs at high redshift in accordance with the sub-mm observations of deep fields. We estimated the total flux of the CIB total to be 23.7 ± 0.9 nW m^{-2} sr^{-1}.
– We estimated the fraction of lensed sources in the sub-mm as a function of the flux and wavelength. This contribution is low ($<10\%$) below 500 μm, but high (up to 50%) around 100 mJy in the mm domain.

– We predicted that the population of very bright dusty galaxies detected by SPT without an IRAS counterpart (Vieira et al. 2010) is essentially composed of lensed sub-mm galaxies. We have also predicted the contribution of the lensed sources to the *Planck* number counts.
– We predict the confusion limits for future missions like SPICA or CCAT.
– We estimated the opacity of the Universe to TeV photons.
– Material of the model (software, tables and predictions) is available online[1].

10. Conclusion

We have demonstrated that it is possible to reproduce the number counts from the mid-IR to the mm domain with a rather simple parametric model that is minimized automatically. Nevertheless, other automatically-tuned models reproduce these counts with different redshift distributions (Le Borgne et al. 2009; Marsden et al. 2011). This suggests that number counts alone are insufficient to uniquely constrain these models. Different observables are thus crucial to discriminate the different parametrizations proposed by the model builders. These constraints are the luminosity functions, the redshift distributions, $P(D)$, and the fluctuations. Future measurements of these quantities and their uncertainties have to be very robust to be used to constrain the next generation of models.

References

Aharonian, F. A., Akhperjanian, A. G., Andronache, M., et al. 1999, A&A, 350, 757
Aharonian, F., Akhperjanian, A., Beilicke, M., et al. 2002, A&A, 393, 89
Aharonian, F., Akhperjanian, A., Beilicke, M., et al. 2003, A&A, 406, L9
Alexander, D. M., Bauer, F. E., Chapman, S. C., et al. 2005, ApJ, 632, 736
Austermann, J. E., Dunlop, J. S., Perera, T. A., et al. 2010, MNRAS, 401, 160
Baugh, C. M. 2006, Reports on Progress in Physics, 69, 3101
Bavouzet, N. 2008, Ph.D. Thesis, Université Paris-Sud 11
Beelen, A., Omont, A., Bavouzet, N., et al. 2008, A&A, 485, 645
Berta, S., Magnelli, B., Lutz, D., et al. 2010, A&A, 518, L30
Bertin, E., Dennefeld, M., & Moshir, M. 1997, A&A, 323, 685
Béthermin, M., Dole, H., Beelen, A., & Aussel, H. 2010a, A&A, 512, A78
Béthermin, M., Dole, H., Cousin, M., & Bavouzet, N. 2010b, A&A, 516, A43
Borys, C., Chapman, S., Halpern, M., & Scott, D. 2003, MNRAS, 344, 385
Caputi, K. I., Lagache, G., Yan, L., et al. 2007, ApJ, 660, 97
Chapin, E. L., Pope, A., Scott, D., et al. 2009, MNRAS, 398, 1793
Chapin, E. L., Chapman, S. C., Coppin, K. E., et al. 2011, MNRAS, 411, 505
Chapman, S. C., Blain, A. W., Smail, I., & Ivison, R. J. 2005, ApJ, 622, 772
Chib, S., & Greenberg, E. 1995, Amer. Stat., 49, 325
Clements, D. L., Rigby, E., Maddox, S., et al. 2010, A&A, 518, L8
Cole, S., Lacey, C. G., Baugh, C. M., & Frenk, C. S. 2000, MNRAS, 319, 168
Condon, J. J. 1974, ApJ, 188, 279
Coppin, K., Chapin, E. L., Mortier, A. M. J., et al. 2006, MNRAS, 372, 1621
Desai, V., Soifer, B. T., Dey, A., et al. 2008, ApJ, 679, 1204
Devlin, M. J., Ade, P. A. R., Aretxaga, I., et al. 2009, Nature, 458, 737
Dole, H., Lagache, G., & Puget, J. 2003, ApJ, 585, 617

---

[1] http://www.ias.u-psud.fr/irgalaxies/

Dole, H., Lagache, G., Puget, J., et al. 2006, A&A, 451, 417
Domínguez, A., Primack, J. R., Rosario, D. J., et al. 2011, MNRAS, 410, 2556
Driver, S. P., Popescu, C. C., Tuffs, R. J., et al. 2008, ApJ, 678, L101
Dunkley, J., Bucher, M., Ferreira, P. G., Moodley, K., & Skordis, C. 2005, MNRAS, 356, 925
Dwek, E., & Krennrich, F. 2005, ApJ, 618, 657
Elbaz, D., Cesarsky, C. J., Fadda, D., et al. 1999, A&A, 351, L37
Engelbracht, C. W., Blaylock, M., Su, K. Y. L., et al. 2007, PASP, 119, 994
Fadda, D., Yan, L., Lagache, G., et al. 2010, ApJ, 719, 425
Fernandez-Conde, N., Lagache, G., Puget, J., & Dole, H. 2008, A&A, 481, 885
Fernandez-Conde, N., Lagache, G., Puget, J., & Dole, H. 2010, A&A, 515, A48
Fixsen, D. J. 2009, ApJ, 707, 916
Franceschini, A., Rodighiero, G., Vaccari, M., et al. 2010, A&A, 517, A74
Frayer, D. T., Sanders, D. B., Surace, J. A., et al. 2009, AJ, 138, 1261
Glenn, J., Conley, A., Béthermin, M., et al. 2010, MNRAS, 409, 109
Gordon, K. D., Engelbracht, C. W., Fadda, D., et al. 2007, PASP, 119, 1019
Gregorich, D. T., Neugebauer, G., Soifer, B. T., Gunn, J. E., & Herter, T. L. 1995, AJ, 110, 259
Greve, T. R., Weiß, A., Walter, F., et al. 2010, ApJ, 719, 483
Griffin, M. J., Abergel, A., Abreu, A., et al. 2010, A&A, 518, L3
Gruppioni, C., Lari, C., Pozzi, F., et al. 2002, MNRAS, 335, 831
Hacking, P., & Houck, J. R. 1987, ApJS, 63, 311
Hall, N. R., Keisler, R., Knox, L., et al. 2010, ApJ, 718, 632
Heitler, W. 1954, Quantum theory of radiation, ed. W. Heitler
Hezaveh, Y. D., & Holder, G. P. 2010, ApJ, submitted [arXiv:1010.0998]
Hogg, D. W. 1999 [arXiv:9905116]
Hopkins, A. M., & Beacom, J. F. 2006, ApJ, 651, 142
Hopwood, R., Serjeant, S., Negrello, M., et al. 2010, ApJ, 716, L45
Imanishi, M. 2009, ApJ, 694, 751
Ishihara, D., Onaka, T., Kataza, H., et al. 2010, A&A, 514, A1
Jauch, J. M., & Rohrlich, F. 1976, The theory of photons and electrons, The relativistic quantum field theory of charged particles with spin one-half, ed. J. M. Jauch, & F. Rohrlich
Jauzac, M., Dole, H., Le Floc'h, E., et al. 2011, A&A, 525, A52
Kennicutt, Jr., R. C. 1998, ApJ, 498, 541
Knudsen, K. K., van der Werf, P. P., & Kneib, J. 2008, MNRAS, 384, 1611
Lacey, C. G., Baugh, C. M., Frenk, C. S., et al. 2010, MNRAS, 443
Lagache, G., Abergel, A., Boulanger, F., Désert, F. X., & Puget, J. 1999, A&A, 344, 322
Lagache, G., Haffner, L. M., Reynolds, R. J., & Tufte, S. L. 2000, A&A, 354, 247
Lagache, G., Dole, H., Puget, J.-L., et al. 2004, ApJS, 154, 112
Lagache, G., Puget, J., & Dole, H. 2005, ARA&A, 43, 727
Lagache, G., Bavouzet, N., Fernandez-Conde, N., et al. 2007, ApJ, 665, L89
Lanzoni, B., Guiderdoni, B., Mamon, G. A., Devriendt, J., & Hatton, S. 2005, MNRAS, 361, 369
Larson, D., Dunkley, J., Hinshaw, G., et al. 2011, ApJS, 192, 16
Le Borgne, D., Elbaz, D., Ocvirk, P., & Pichon, C. 2009, A&A, 504, 727
Le Floc'h, E., Papovich, C., Dole, H., et al. 2005, ApJ, 632, 169
Le Floc'h, E., Aussel, H., Ilbert, O., et al. 2009, ApJ, 703, 222
Lima, M., Jain, B., Devlin, M., & Aguirre, J. 2010, ApJ, 717, L31
Lonsdale, C. J., Hacking, P. B., Conrow, T. P., & Rowan-Robinson, M. 1990, ApJ, 358, 60

Magnelli, B., Elbaz, D., Chary, R. R., et al. 2009, A&A, 496, 57
Marsden, G., Ade, P. A. R., Bock, J. J., et al. 2009, ApJ, 707, 1729
Marsden, G., Chapin, E. L., Halpern, M., et al. 2011, ApJ, submitted [arXiv:1010.1176]
Matsuura, S., Shirahata, M., Kawada, M., et al. 2011, ApJ, submitted [arXiv:1002.3674]
Miville-Deschênes, M., Lagache, G., & Puget, J. 2002, A&A, 393, 749
Negrello, M., Perrotta, F., González-Nuevo, J., et al. 2007, MNRAS, 377, 1557
Negrello, M., Hopwood, R., De Zotti, G., et al. 2010, Science, 330, 800
Nguyen, H. T., Schulz, B., Levenson, L., et al. 2010, A&A, 518, L5
Oliver, S. J., Wang, L., Smith, A. J., et al. 2010, A&A, 518, L21
Papovich, C., Dole, H., Egami, E., et al. 2004, ApJS, 154, 70
Pascale, E., Ade, P. A. R., Bock, J. J., et al. 2008, ApJ, 681, 400
Pascale, E., Ade, P. A. R., Bock, J. J., et al. 2009, ApJ, 707, 1740
Patanchon, G., Ade, P. A. R., Bock, J. J., et al. 2009, ApJ, 707, 1750
Pearson, C. P., Oyabu, S., Wada, T., et al. 2010, A&A, 514, A8
Perrotta, F., Baccigalupi, C., Bartelmann, M., De Zotti, G., & Granato, G. L. 2002, MNRAS, 329, 445
Perrotta, F., Magliocchetti, M., Baccigalupi, C., et al. 2001, unpublished [arXiv:astro-ph/0111239]
Pilbratt, G. L., Riedinger, J. R., Passvogel, T., et al. 2010, A&A, 518, L1
Puget, J., Abergel, A., Bernard, J., et al. 1996, A&A, 308, L5
Reddy, N. A., Steidel, C. C., Pettini, M., et al. 2008, ApJS, 175, 48
Reed, D. S., Bower, R., Frenk, C. S., Jenkins, A., & Theuns, T. 2007, MNRAS, 374, 2
Renault, C., Barrau, A., Lagache, G., & Puget, J. 2001, A&A, 371, 771
Rodighiero, G., Vaccari, M., Franceschini, A., et al. 2010, A&A, 515, A8
Rowan-Robinson, M. 2009, MNRAS, 394, 117
Rowan-Robinson, M., Hughes, J., Vedi, K., & Walker, D. W. 1990, MNRAS, 246, 273
Saunders, W., Rowan-Robinson, M., Lawrence, A., et al. 1990, MNRAS, 242, 318
Scott, S. E., Dunlop, J. S., & Serjeant, S. 2006, MNRAS, 370, 1057
Scott, K. S., Yun, M. S., Wilson, G. W., et al. 2010, MNRAS, 405, 2260
Shupe, D. L., Rowan-Robinson, M., Lonsdale, C. J., et al. 2008, AJ, 135, 1050
Smail, I., Ivison, R. J., Blain, A. W., & Kneib, J. 2002, MNRAS, 331, 495
Soifer, B. T., & Neugebauer, G. 1991, AJ, 101, 354
Stansberry, J. A., Gordon, K. D., Bhattacharya, B., et al. 2007, PASP, 119, 1038
Stecker, F. W., & de Jager, O. C. 1997, ApJ, 476, 712
Swinyard, B. M., Ade, P., Baluteau, J., et al. 2010, A&A, 518, L4
Takeuchi, T. T., & Ishii, T. T. 2004, ApJ, 604, 40
Teplitz, H. I., Chary, R., Elbaz, D., et al. 2011, AJ, 141, 1
Truch, M. D. P., Ade, P. A. R., Bock, J. J., et al. 2009, ApJ, 707, 1723
Vaccari, M., Marchetti, L., Franceschini, A., et al. 2010, A&A, 518, L20
Valiante, E., Lutz, D., Sturm, E., Genzel, R., & Chapin, E. L. 2009, ApJ, 701, 1814
Vieira, J. D., Crawford, T. M., Switzer, E. R., et al. 2010, ApJ, 719, 763
Viero, M. P., Ade, P. A. R., Bock, J. J., et al. 2009, ApJ, 707, 1766
Weiß, A., Kovács, A., Coppin, K., et al. 2009, ApJ, 707, 1201
Wilman, R. J., Jarvis, M. J., Mauch, T., Rawlings, S., & Hickey, S. 2010, MNRAS, accepted [arXiv:1002.1112]
Younger, J. D., & Hopkins, P. F. 2011, MNRAS, 410, 2180
Zemcov, M., Blain, A., Halpern, M., & Levenson, L. 2010, ApJ, 721, 424